Experiments in Fluids (2026) 67:78
https://doi.org/10.1007/s00348-026-04229-8

RESEARCH ARTICLE

Instantaneous pressure reconstruction from PIV in compressible launcher conditions

A. D'Aguanno[1,2] · F. F. J. Schrijer[1] · B. W. van Oudheusden[1]

Received: 12 December 2025 / Revised: 22 April 2026 / Accepted: 24 April 2026

Abstract

Unsteady pressure fluctuations in transonic launcher configurations represent a major challenge, driven by shock oscillations, flow separation, and compressibility effects. To address these phenomena, this work presents and validates a methodology for reconstructing instantaneous pressure fields from planar (2D2C) and stereo particle image velocimetry (2D3C PIV) data using Taylor's hypothesis. The approach is first assessed using a simulated PIV dataset of an axisymmetric backward-facing step, representing a launcher base flow configuration. In this case, the Taylor-based pressure reconstruction is validated against reference data and compared with results from a hypothetical time-resolved pressure reconstruction, demonstrating the accuracy of the method.

The methodology is then applied to wind tunnel PIV data of a VEGA-like hammerhead launcher model at Mach 0.8 and zero angle of attack. Hammerhead configurations, characterized by payload fairings with a larger diameter than the main body, are particularly prone to separation and intense pressure fluctuations in the transonic ascent phase. The reconstructed pressure fields are analyzed together with unsteady transducer data, providing a general characterization of the flow features (oscillating shock, separation, and reattachment) and showing very good agreement for instantaneous, mean, and fluctuating components ($\Delta C_{p\ avg} \sim 0.01$–$0.02$; $\Delta C_{p\ std} \sim 0.02$). Finally, the analysis highlights the impact of neglecting out-of-plane velocity components, which introduces noticeable discrepancies in separated regions.

Graphical Abstract

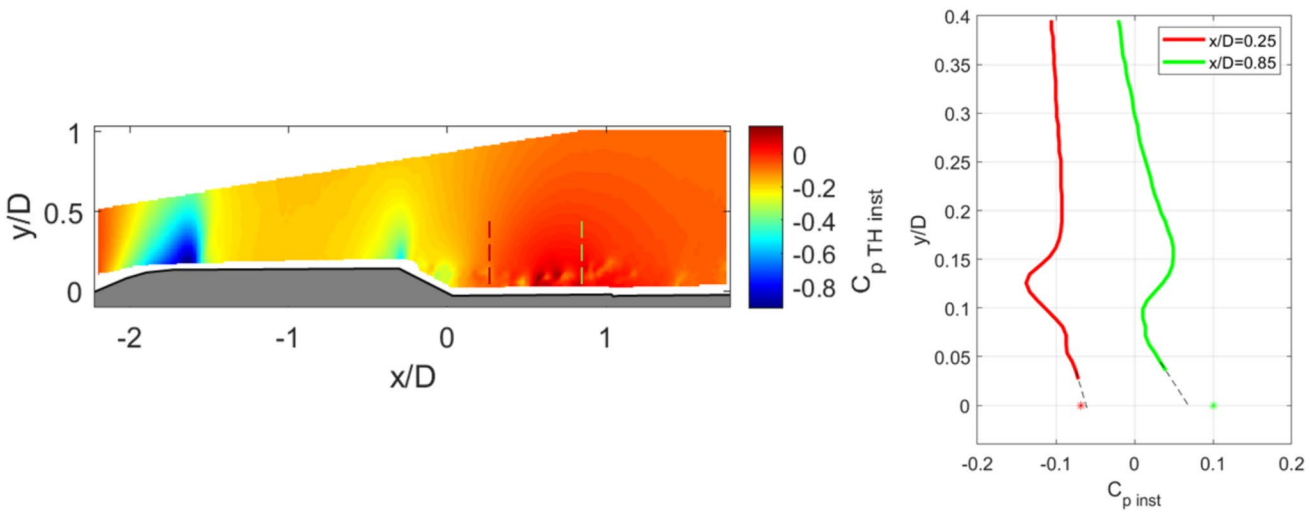

Abbreviations

PIV	Particle image velocimetry
PSP	Pressure sensitive paint
TR	Time-resolved
TH	Taylor's hypothesis
2D, 3D	Two/ three-dimensional
FOV	Field of view
BFS	Backward facing step

Extended author information available on the last page of the article

Published online: 05 June 2026

List of symbols

t	Time [s]
T	Static temperature [K]
p	Static pressure [bar]
C_p	Pressure coefficient
ρ	Static density [kg/m^3]
Ma	Mach number [-]
$\boldsymbol{U}_\mathbf{c}$ (U_c, V_c, W_c)	Convection velocity vector
$\boldsymbol{u}$ (u, v, w)	Velocity vector
V	Velocity magnitude
R	Specific gas constant
γ	Heat capacity ratio
Re	Reynolds number
x, y, z	Cartesian coordinates [m]
D	Payload diameter [m]
d	Second stage diameter [m]
h	Step height [m]
BT	Boat tail angle [°]
f	Acquisition frequency [Hz]
τ	Correlation time delay [s]
ϵ	Error

Subscripts and superscripts

∞	Freestream quantities
0	Total quantities
‘	Fluctuating quantity
avg	Average quantity
std	Standard deviation quantity
inst	Instantaneous quantity

1 Introduction

Unsteady aerodynamic loads on launcher payload fairings can pose serious risks for structural integrity, payload safety, and overall vehicle stability. These effects are particularly critical in transonic conditions, where shock oscillations, flow separation, and associated pressure fluctuations become severe. The present study addresses this problem by focusing on pressure reconstruction from particle image velocimetry (PIV) measurements in a transonic launcher environment.

With the need for increased payload volume, launcher fairings have become larger in size, resulting in so-called hammerhead configurations (see Fig. 1, where the fairing diameter is about 60% larger than the connecting upper stage of the launcher). For freestream Mach numbers close to and above 0.7, a local region of supersonic velocity is induced with associated shock formation (Coe and Nute (1962); D'Aguanno et al. (2025)). These shocks interact with the boundary layer developing over the launcher, causing flow unsteadiness such as buffet. This effect is amplified at the rear part of the fairing, where the flow tends to separate. The separation and reattachment of the flow around the model are responsible for additional unsteadiness and associated time-varying pressure loads.

In order to experimentally evaluate the unsteady pressures and loads, wind tunnel experiments are needed at representative Mach and Reynolds numbers. Typically, these loads can be evaluated through load balances and/or unsteady pressure sensors. An example of unsteady pressure sensor measurements was presented in Panda et al. (2018), which highlights the presence of high-pressure fluctuations in correspondence with the shockwave structures and in proximity of the reattachment area. Although unsteady pressure transducers provide accurate measurements of pressure fluctuations, their application is inherently limited by their cost and the finite physical size of the sensors. At model scale, this constraint severely restricts the achievable spatial resolution, making it difficult to capture the detailed pressure field associated with shock motion and separated flow regions. As an alternative, unsteady pressure-sensitive paint (PSP) can be employed to obtain spatially resolved surface pressure measurements (e.g. Schuster et al. 2016). Both unsteady pressure transducers and PSP provide valuable information on the surface pressure distribution, which is directly relevant for assessing aerodynamic loads acting on the vehicle. However, these techniques do not provide access to the underlying flow field responsible for the observed pressure fluctuations. In this context, particle-based flow field measurement techniques offer a complementary capability, as they enable the characterization of the velocity field and associated flow structures, while also allowing the reconstruction of pressure fields.

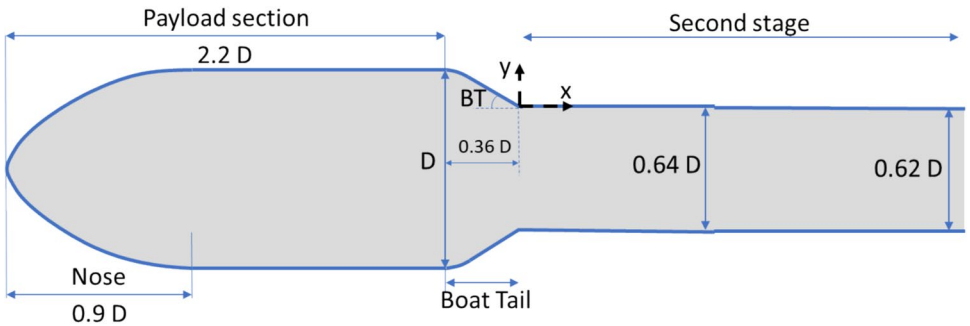

Fig. 1 Sketch of hammerhead VEGA-like launcher model with dimensions ($D = 50$ mm)

The operating principle and methodology for this approach is described in the review of van Oudheusden (2013) and the implementation for the present investigation is discussed in more detail in Sect. 2. This will then provide a simultaneous characterization of the flow field and corresponding pressure field.

It has been demonstrated that for incompressible flows it is possible to obtain unsteady (i.e. instantaneous) pressure from time-resolved PIV in turbulent boundary layers (Ghaemi et al. (2012)), around blunt bodies, in jets, etc. (Pröbsting et al. (2013); de Kat (2012); van Gent et al. (2016); McClure and Yarusevych (2017)). However, pressure determination is not as straightforward for compressible flows (van Oudheusden (2008)), and it is still in the development phase. Apart from a variety of technical challenges inherent to high-speed wind tunnel facilities (tunnel vibrations, limited optical access), the very short characteristic time scales in general preclude the achievement of time-resolved PIV measurements. Furthermore, the fact that density can no longer be considered as constant has to be accounted for. For the mean pressure field, it has been demonstrated that good results can be obtained, under realistic experimental conditions, for transonic base-flows and shock interactions (see van Oudheusden (2013) and van Gent et al. (2018)). However, to obtain instantaneous pressure in order to characterize pressure fluctuations, additional work is needed.

Although significant technological progress has been achieved in recent years in both camera and laser systems, the applicability of time-resolved PIV-based pressure reconstruction in compressible conditions remains primarily constrained by illumination capabilities. As discussed by Geschwindner et al. (2022), current high-energy industrial laser systems are still not capable of sustaining sufficiently high pulse energy at repetition rates beyond approximately 150 kHz. At the short inter-frame times required for transonic flows (Δt on the order of a few microseconds), this limitation restricts the achievable sampling frequency for fully time-resolved measurements in large-scale wind tunnel environments.

Nevertheless, while the available laser repetition rates may be insufficient to fully resolve the smallest temporal scales of transonic flows or to directly capture the instantaneous acceleration field, relatively low-frequency unsteady phenomena (such as shock oscillations in transonic buffet or shock–boundary layer interactions) can already be temporally resolved.

A possibility to directly measure the acceleration field is by using a four-pulse system (Schreyer et al. (2015)). For this specific set-up, two PIV systems are generally used (three sets of four cameras and two double-pulse laser systems in the tomo-PIV measurements of Lynch et al. (2014)), in such a way that sets of multiple, time-correlated velocity fields can be used to compute the acceleration field. However, neither the spectrum of the acceleration field nor of the velocity field can be retrieved. It is also worth adding that, in view of the number of additional hardware components, their alignment and synchronization, such a set-up is characterized as being complicated and expensive, since generally the operation of two PIV systems is required.

Furthermore, the technical limitations described above make conventional time-resolved Lagrangian and Eulerian approaches for determining the acceleration unfeasible. Therefore, a pressure reconstruction approach based on modelling the acceleration term in the momentum equation seems most attractive for implementation in industrial compressible flow environments, notwithstanding its lower accuracy. Such approaches are also referred to as single snapshot approaches, since the instantaneous pressure is evaluated from information of a single velocity field (van Gent et al. (2017)). This study adopts a reconstruction approach based on Taylor's hypothesis (see de Kat and Ganapathisubramani (2013)). The objective is twofold: first, to validate the methodology against synthetic compressible data, and second, to apply it to wind tunnel experiments on a VEGA-like hammerhead launcher model. This allows for a simultaneous characterization of velocity and pressure fields, together with a direct comparison to unsteady pressure transducer data, thereby assessing the applicability and limitations of Taylor-based pressure reconstruction in a realistic compressible environment. In doing so, the study both establishes and validates the pressure reconstruction procedure for experimental data and provides new insight into the unsteady aerodynamics of transonic launcher flows.

2 Pressure reconstruction formulation

Sufficiently far away from the model the flow can be considered inviscid and adiabatic, hence, the isentropic relations can be used as boundary conditions for the temperature and the pressure field.

These considerations are not valid in wake areas behind models, where the flow is rotational. However, using the approximation that viscous contribution to the momentum equation is only relevant in the region close to the model surface, as confirmed in van Oudheusden et al. (2007a) and Ghaemi et al. (2012), the differential form of the momentum equation allows to obtain the local pressure gradient, as:

$$\nabla p = -\rho \frac{\mathrm{D}\mathbf{u}}{Dt} \tag{1}$$

The variable density term can be eliminated by a procedure involving the perfect gas equation ($\rho = p/RT$) combined with the steady, adiabatic energy equation (equivalent to constant total temperature), such that:

$$T = \frac{p}{\rho R} = \frac{V_\infty{}^2 + \frac{\gamma-1}{2} Ma_\infty{}^2 \left(V_\infty{}^2 - V^2\right)}{\gamma R Ma_\infty{}^2} \tag{2}$$

Combining this result with the momentum Eq. (1) relates the pressure gradient field to the velocity field (van Oudheusden et al. (2007b):

$$\nabla \ln\left(\frac{p}{p_\infty}\right) = -\frac{1}{\mathrm{RT}} \bullet \frac{D\boldsymbol{u}}{\mathrm{Dt}} = -\frac{\gamma Ma_\infty{}^2}{V_\infty{}^2 + \frac{\gamma-1}{2} Ma_\infty{}^2 \left(V_\infty{}^2 - V^2\right)} \bullet \frac{\mathrm{D}\mathbf{u}}{\mathrm{Dt}} \tag{3}$$

As previously anticipated, since the exact determination of the acceleration term (in the form of the material derivative of the velocity field, D**u**/Dt) is not feasible in transonic conditions, in this study it was modelled using Taylor's hypothesis (TH, de Kat and Ganapathisubramani (2013), Laskari et al. (2016)). According to this hypothesis turbulent structures advect in the flow in a "frozen" state, considering that advection due to turbulent circulation is small, with $\boldsymbol{U_c}(U_c, V_c, W_c, t)$ being the local convection velocity of the perturbations. Decomposing the velocity field in a mean and a fluctuation component, $\boldsymbol{u} = \boldsymbol{U} + \boldsymbol{u\prime}$, the following expression is obtained:

$$\frac{\mathrm{D}\mathbf{u}'}{\mathrm{Dt}} = \frac{\partial \boldsymbol{u\prime}}{\partial t} + \left(\boldsymbol{U_c} \bullet \nabla\right)\boldsymbol{u\prime} \approx 0 \rightarrow \frac{\partial \boldsymbol{u\prime}}{\partial t} \approx -\left(\boldsymbol{U_c} \bullet \nabla\right)\boldsymbol{u\prime} \tag{4}$$

Under this hypothesis it is possible to retrieve temporal information on the basis of spatial information, such that the equation for the pressure gradient can be rewritten as:

$$\nabla \ln\left(\frac{p_{TH}}{p_\infty}\right) = -\frac{1}{RT} \bullet \frac{\mathrm{D}\mathbf{u}}{\mathrm{Dt}} = -\frac{\gamma Ma_\infty{}^2}{V_\infty{}^2 + \frac{\gamma-1}{2} Ma_\infty{}^2 \left(V_\infty{}^2 - V^2\right)} \bullet \left(-\left(\boldsymbol{U_c} \bullet \nabla\right)\boldsymbol{u\prime} + \boldsymbol{u} \bullet \nabla \boldsymbol{u}\right) \tag{5}$$

de Kat and Ganapathisubramani (2013) demonstrated that Taylor's hypothesis performs well in flows with weak turbulent fluctuations, whereas in strongly turbulent or separated flows the associated errors become higher. In several subsequent studies, the convection velocity of turbulent structures has been approximated by the local mean velocity (e.g. Laskari et al. (2016); van Gent et al. (2017)). However, this approximation is not generally valid in the presence of shear layers, as shown by Lin (1953) and later confirmed by Davoust and Jacquin (2011) among others.

Regarding the dimensionality of PIV data, Taylor's hypothesis was first successfully applied to volumetric measurements (de Kat and Ganapathisubramani, (2013)), and more recently to 2D planar PIV (Van der Kindere et al., (2019)). In the latter study, the 2D assumption introduced an error of about 5–10% in the instantaneous pressure field compared to the 3D case, while its impact on the mean pressure reconstruction was even much smaller. The same work also showed that the Taylor-based approach produced results in good agreement with 2D Eulerian and pseudo-Lagrangian methods, but with a smoother p_{rms} (pressure rms) profile and greater robustness to measurement noise. This outcome is consistent with the fact that Eulerian and Lagrangian reconstructions are affected by noise in both spatial and temporal gradients, whereas Taylor's hypothesis relies only on spatial information.

A primary objective of the current study is to assess the feasibility of instantaneous pressure reconstruction in industrial wind-tunnel environments. Therefore, only 2D-2C (planar) and 2D-3C (stereo) particle image velocimetry measurements will be taken into account, in view of the complexity of conducting volumetric PIV experiments. In view of this the out-of-plane derivatives are neglected resulting in the following simplified relations:

$$\frac{\partial}{\partial x}\ln\left(\frac{p_{TH}}{p_\infty}\right) = -\frac{\gamma Ma_\infty{}^2}{V_\infty{}^2 + \frac{\gamma-1}{2} M_\infty{}^2 \left(V_\infty{}^2 - V^2\right)} \bullet \left(-U_c \frac{\partial u\prime}{\partial x} - V_c \frac{\partial u\prime}{\partial y} + u\frac{\partial u}{\partial x} + v\frac{\partial u}{\partial y}\right) \tag{6}$$

$$\frac{\partial}{\partial y}\ln\left(\frac{p_{TH}}{p_\infty}\right) = -\frac{\gamma Ma_\infty{}^2}{V_\infty{}^2 + \frac{\gamma-1}{2} Ma_\infty{}^2 \left(V_\infty{}^2 - V^2\right)} \bullet \left(-U_c \frac{\partial v\prime}{\partial x} - V_c \frac{\partial v\prime}{\partial y} + u\frac{\partial v}{\partial x} + v\frac{\partial v}{\partial y}\right) \tag{7}$$

It is worth mentioning that in case of stereo PIV measurements, all three velocity components are retrieved in the measurement plane, therefore the square of the velocity magnitude is evaluated as $V^2 = u^2 + v^2 + w^2$.

From Eqs. 6, 7 the pressure field can be obtained either with spatial-marching integration or by solving the corresponding Poisson equation (see van Oudheusden (2013)).

In case of flows that contain shock waves, Souverein et al. (2007) followed an approach where the shockwave was first explicitly localized by means of the divergence field and treated separately by applying the theoretical shock relations, while in the remaining field of view (FOV) the field was integrated according to van Oudheusden (2013). In a further study, van Oudheusden (2008) showed that this spatial integration procedure may also be applied across a shockwave, provided that a conservative formulation of the momentum equation is used.

In this study the pressure field was computed by solving a Poisson equation (see Charonko et al. (2010), de Kat and van Oudheusden, (2012)) which is obtained by applying the divergence to the gradient of the (logarithm of the) pressure:

$$\begin{aligned}\nabla \bullet \nabla \ln\left(\frac{p_{TH}}{p_\infty}\right) &= \nabla^2\left(\ln\left(\frac{p_{TH}}{p_\infty}\right)\right) \\ &= \frac{\partial^2}{\partial x^2}\left(\ln\left(\frac{p_{TH}}{p_\infty}\right)\right) + \frac{\partial^2}{\partial y^2}\left(\ln\left(\frac{p_{TH}}{p_\infty}\right)\right)\end{aligned} \tag{8}$$

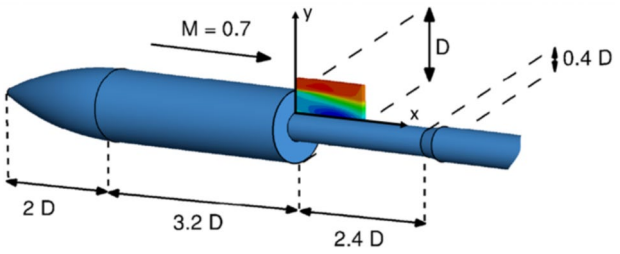

Fig. 2 Sketch of the model geometry of the synthetic PIV experiment with field of view. Image from van Gent et al. (2017)

The choice for integrating the pressure in this way comes from the fact that spatial marching methods have a higher error accumulation (and are less robust) in presence of velocity errors with respect to the Poisson approach (see McClure and Yarusevich (2017)).

To solve the Poisson equation, Neumann boundary conditions were imposed on all sides except for the top surface of the domain (see Fig. 2) where the isentropic pressure values were used as a Dirichlet boundary condition. The Neumann conditions correspond to specifying the normal pressure gradient derived from the momentum equation, which is consistent with the measured velocity field and avoids imposing artificial pressure levels at the domain boundaries. Since the Poisson problem requires one reference pressure to ensure uniqueness of the solution, a Dirichlet condition is introduced at the top boundary, where the flow is assumed to be nearly uniform and weakly affected by separation or shock motion, making the isentropic approximation appropriate. In this study, the Poisson equation was solved with the same approach as reported in Ragni et al. (2011a, b) by discretizing the Poisson equation with a second order finite difference scheme and inverting a linear system of equations.

In terms of discretization, the spatial derivatives were obtained with a central difference scheme in the internal points and forward and backward schemes at the boundaries.

It is worth mentioning that although the Taylor's hypothesis approach has been successfully applied to subsonic experimental data and compressible volumetric synthetic data (van Gent et al. (2017)), it has not yet been applied to experimental compressible velocity data.

3 Methodology

3.1 Synthetic data-set

To validate the approach described in Sect. 2, synthetic PIV data from the numerical simulations described in van Gent et al. (2017) have been used. The flow geometry of this synthetic experiment consists of an axisymmetric backward-facing step (BFS) resembling the model which will be experimentally investigated in this study.

Figure 2 shows the model geometry, and the virtual measurement volume of the synthetic experiment. The model has a forebody with a diameter (D) of 50 mm and an afterbody diameter ($d = 0.4D$) of 20 mm, as a result, the axisymmetric step height is 15 mm. The general dimensions are comparable to the experimental model investigated in the present study (see Table 1, where also other characteristic information is summarized). The freestream Mach number (Ma_∞) is 0.7, the total pressure (p_0) is 200 kPa and the total temperature (T_0) 285 K. In view of the availability of the synthetic data, for this case the pressure reconstruction strategies are not bounded by technological limitations as time-resolved velocity sequences are available. This allows the pressure reconstruction obtained with the Taylor's hypothesis to be compared to an ideal Eulerian time-resolved pressure reconstruction method (TR) (see van Oudheusden (2013)).

Although the synthetic data were obtained in a volume (60 mm × 24 mm × 4 mm) with tomo-PIV processing, only the three velocity components in the central measurement plane ($z = 0$) were considered to replicate the same typology of (stereo-) data that were obtained from the experimental campaign of the current investigation. The final FOV of the synthetic PIV data is restricted to the region immediately downstream of the backward-facing step, and the data have a comparable spatial resolution (vector spacing of 0.35 mm) as the current PIV experiment.

3.2 Experimental investigation

The current experimental study was performed in the transonic-supersonic wind tunnel (TST 27) of TU Delft, which is a blowdown wind tunnel with a test section that is 255 mm high and 280 mm wide. The experiments were conducted with a total pressure $p_0 = 200$ kPa, total temperature $T_0 = 288$ K and a freestream Mach number $Ma_\infty = 0.80$.

The experimental geometry tested in this study was provided by the European Space Agency (ESA) and corresponds to a VEGA-like launcher configuration and tested at an angle of attack of $\alpha = 0°$. A schematic of the model, including characteristic dimensions, is shown in Fig. 3. It features an ogive nose, curved edges at the payload–boat tail junction (grey region in Fig. 3), and a conical boat tail (BT) with a 30° inclination. The model has a payload diameter $D = 50$ mm and a second-stage diameter $d = 32$ mm, resulting in a step height $h = (D - d)/2 = 9$ mm. The configuration bears a similarity to the Coe and Nute (1962) configuration (BT = 34°), for which a large dataset for transonic Mach numbers (particularly for $Ma = 0.8$ and $\alpha = 0$–4°) is available.

In order to trigger turbulent boundary layer transition over the launcher model, a transition trip was added at 20% of the nose length. This position corresponds to approximately 5%

Table 1 PIV settings for the experimental and synthetic data-sets

Parameter	PIV experiment	Synthetic PIV data-set
Total pressure (p_0)	200 kPa	200 kPa
Total temperature (T_0)	288 K	285 K
Freestream velocity (V_∞)	256 m/s	226 m/s
Freestream mach number (Ma_∞)	0.8	0.7
Model diameter (D)	50 mm	50 mm
Step height (h)	9 mm	15 mm
Step type	30° BT with rounded corner	Sharp BFS
Camera	4 × sCMOS 5MP	4 × virtual camera
Lens focal length	105 mm	75 mm (virtual)
Acquisition frequency (f)	15 Hz	500 kHz
Number of images per test case	1000	41
Combined resolution (stitched raw images)	4500 × 1800 pix	1624 × 800 pix
Pulse separation	3 µs	2 µs
Combined field of view	200 mm × 50 mm	60 mm × 24 mm × 4 mm
PIV configuration	Stereo/ Planar	Tomo
Final window size	48 × 48 pix	32 vox
Window overlap	75%	75%
Vector spacing	0.45 mm	0.35 mm
Cross-correlation velocity uncertainty	1.5 m/s	2.2 m/s

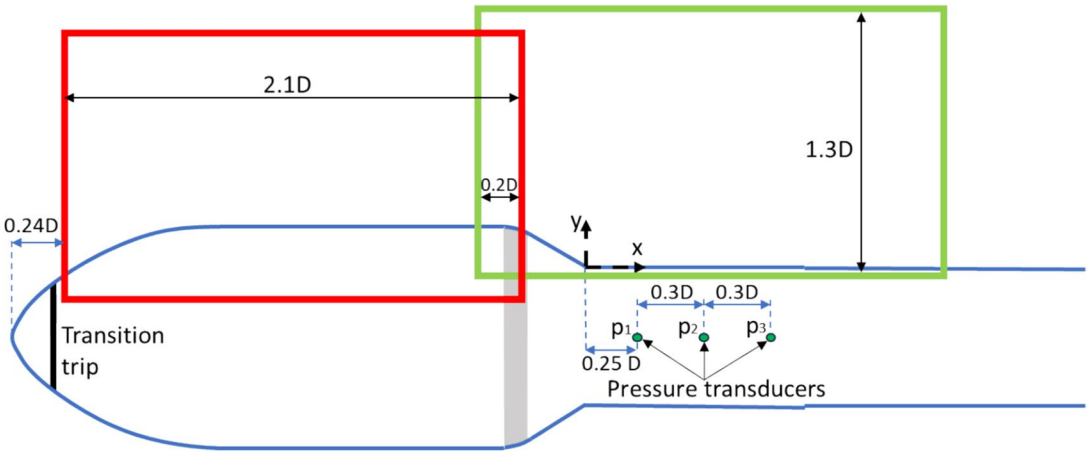

Fig. 3 Side view of PIV field of views

of the entire model length, a location suggested by Goin and Pope (1965). In this study, the transition trip consists of a 1 mm wide, 0.12 mm high strip of carborundum particles (particle size of 14 µm).

The model was equipped with three unsteady pressure transducers (Endevco Model 8507C) which are located at 25, 55, 85%D downstream of the boat tail bottom corner, as indicated in Fig. 3 with p_1, p_2, p_3. These sensors were used to locally validate the pressure data obtained from the PIV measurements. Unfortunately, the second pressure transducer only provided pressure fluctuations and no absolute values due to a leaking membrane.

For the PIV measurements, four LaVision sCMOS 5 MP cameras (resolution 2560 × 2160 pixels) were used, equipped with 105 mm lenses set to an f-stop of 8. The cameras were operated in double-pulse mode with a pulse separation of $\Delta t = 3$ µs in a stereo-PIV configuration. Two equally sized and overlapping fields of views were imaged (see Fig. 3), and a total of 1000 image pairs per camera were acquired. In each camera group, one camera was oriented in-plane with the FOV, while the second was inclined by 30° and fitted with a scheimpflug adapter (see Fig. 4). This configuration was chosen to facilitate the comparison of pressure reconstruction results between planar PIV (2D2C) and those obtained with stereo-PIV (2D3C) data (which also captures

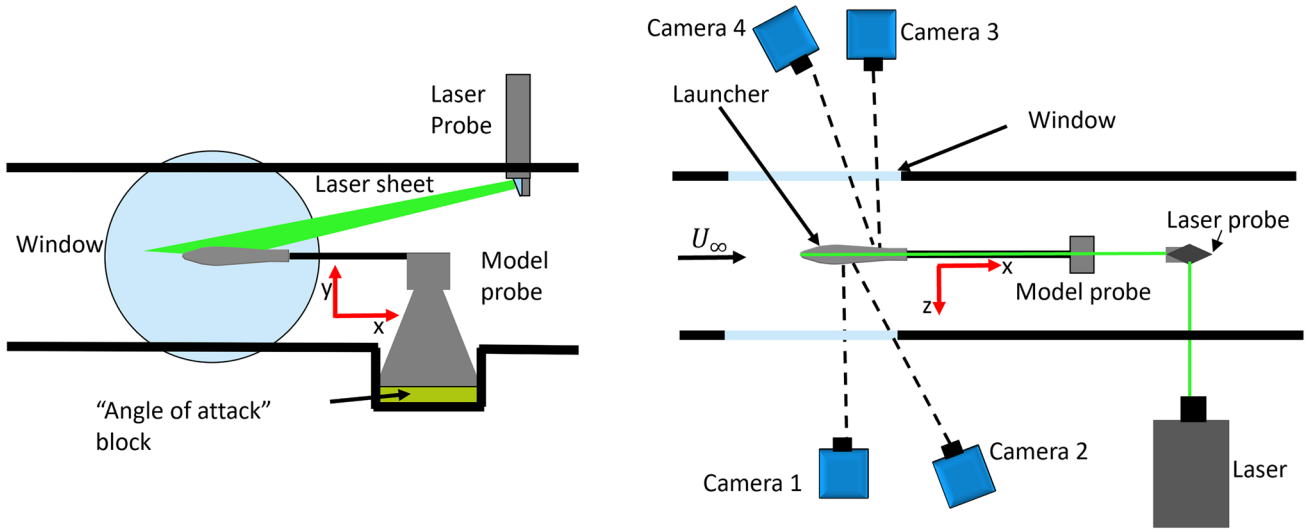

Fig. 4 Side (left) and top view (right) of PIV set-up

the out-of-plane velocity component, but not the out-of-plane gradients). The setup resulted in a combined field of view in the chordwise-vertical plane which is 200 mm long and 50 mm high. Two cameras were centered on the nose area while the remaining two observed the boat tail and reattachment region. This configuration enabled a simultaneous visualization of the shockwaves on the fairing, the separation area and the reattachment region. Due to the limited optical access into the test section, the cameras imaging the nose region and those observing the boat-tail region were arranged on opposite sides of the wind tunnel.

DEHS (Di-Ethyl-Hexyl-Sebacate) oil was used as flow seeding, characterized by a relaxation time of 2 µs (Ragni et al. (2011a, b)) and a median particle size of 1 µm. The particles were illuminated by a 1 mm thick light sheet generated by a dual cavity laser (Quantel Evergreen 200 laser) at a repetition frequency of 15 Hz. The laser beam was introduced into the wind tunnel by means of a laser probe, from the top wall of the wind tunnel (see Fig. 4, left). To ensure a synchronization between cameras and laser, a LaVision programmable timing unit was employed.

The PIV images were collected and processed in Davis 10.0.5. A Butterworth filter with a kernel of 7 images (as suggested by Sciacchitano and Scarano (2014)) was applied to reduce laser reflections and maximize the signal-to-noise ratio. The velocity field was then extracted in two ways, either using stereo or planar cross-correlation. In both cases, a multi-pass approach was chosen, starting with 2 passes with a window size of 96×96 pixels and three subsequent steps with a circular window size of 48×48 pixels. A window overlap of 75% resulted in a vector spacing of 0.45 mm, which corresponds to 0.9% D. Finally, the universal outlier detection with a threshold value of 2 was utilized to eliminate outliers. Further processing, including the pressure reconstruction, was performed in Matlab. The main PIV settings are summarized in Table 1.

This PIV procedure is subject to various sources of uncertainty (for more details see D'Aguanno (2023)). For example, the cross-correlation procedure has an uncertainty lower than 0.1 pixels, which results in a corresponding uncertainty on the velocity lower than 1.5 m/s. Additionally, the velocity estimation is affected by the relaxation time of the seeding particles (2 µs for the seeding used, see above). This effect can cause local uncertainty values as high as 50 m/s in the vicinity of shock waves; however, this uncertainty is negligible in the remaining part of the FOV.

To evaluate a first estimate of the propagation of velocity uncertainty into the pressure coefficient, the isentropic relation between velocity and pressure can be considered. For small perturbations, the uncertainty in C_p scales approximately as $\Delta C_p \approx -2\,\Delta \mathbf{u}\,/\mathbf{u}$ (van Oudheusden 2008). Given a relative uncertainty in velocity lower than 1% in most of the field of view (outside shock regions), the resulting uncertainty in C_p is expected to remain below approximately 0.02.

The estimation of C_p using Taylor's hypothesis depends on two main factors: (i) the uncertainty in the local mean velocity field obtained from PIV measurements, and (ii) the approximation of the convection velocity by the local mean velocity (Laskari et al. 2016). The uncertainty of the mean velocity is governed by the statistical convergence of the PIV dataset. Based on the number of acquired samples, the statistical uncertainty of the mean velocity remains below 1 m/s over most of the field of view and reaches approximately 3 m/s for the streamwise component within the wake region. This corresponds to a maximum uncertainty of about 2%

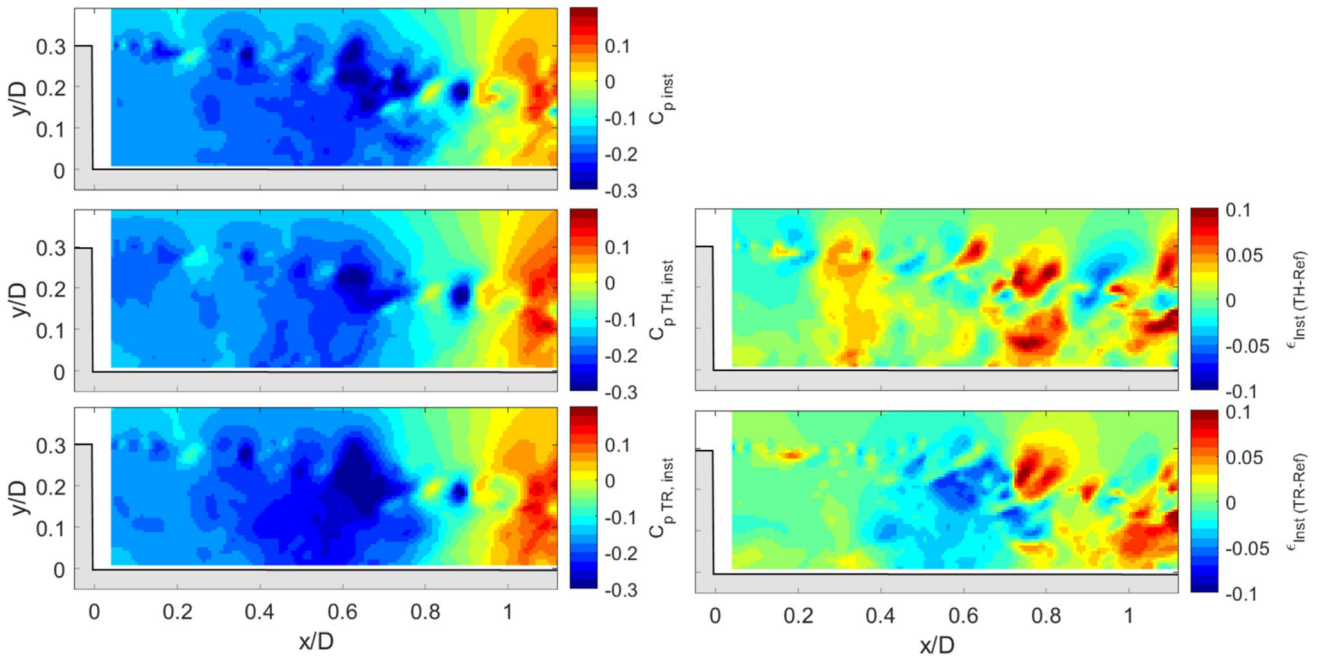

Fig. 5 Instantaneous static pressure coefficient (synthetic data at $Ma = 0.7$) for reference data (top left), Taylor's hypothesis approach (center left) and time-resolved approach (bottom left). The discrepancies between the TH reconstruction and the reference data (center right) and between the TR reconstruction and the reference data (bottom right) are also reported

of the local convection velocity and represents the primary measurement-related contribution to the uncertainty in U_c.

In contrast, quantifying the uncertainty associated with the modeling assumption $U_c(x,y) \approx U_{\text{avg}}(x,y)$ is more challenging when relying solely on experimental data. In Laskari et al. (2016), this contribution was assessed using DNS data, enabling a controlled evaluation of the Taylor's hypothesis approximation. In the present experimental study, its impact is therefore discussed in the context of the observed ΔC_p discrepancies. Additionally, Sect. 6.2 provides a comparison between the convection velocity estimated from pressure transducer signals and that obtained from the PIV data, offering further insight into the validity of this assumption.

4 Validation with synthetic data

In this section, the proposed Taylor's Hypothesis pressure reconstruction approach is assessed using the synthetic PIV dataset described in Sect. 3.1. The purpose of this validation is twofold. First, the dataset provides a reference pressure field directly from the numerical simulation (Ref), enabling a quantitative error assessment of the reconstructed pressure. Second, owing to the high synthetic acquisition frequency, an ideal time-resolved pressure reconstruction can be performed. This allows a direct comparison between the proposed TH method and a state-of-the-art time-resolved approach under controlled conditions.

Figure 5 presents a sample instantaneous pressure field from the reference solution, together with the corresponding pressure reconstructed using the TH and TR approaches. The field of view encompasses the base flow of the launcher-like geometry, immediately downstream of the backward-facing step. Vortical structures emerge from $y/D = 0.3$, corresponding to the upper corner of the BFS, and convect downstream within the shear layer.

Qualitatively, the TH approach reproduces the main features of the instantaneous pressure field. Lower pressure regions are captured up to approximately $x/D = 0.8$, with higher pressure levels further downstream as the flow approaches reattachment (located outside the present FOV at $x/D \approx 1.3$, see van Gent et al. 2017). While the overall agreement is good, a quantitative comparison indicates that the TR method provides a slightly improved prediction of the extrema of C_p.

To quantify the reconstruction accuracy, the instantaneous error fields are defined as $\epsilon_{TH\text{-}Ref} = C_{p,TH} - C_{p,\,Ref}$ *and* $\epsilon_{TR\text{-}Ref} = C_{p,TR} - C_{p,\,Ref}$.

As shown in Fig. 5 (right), the TH approach exhibits typical errors of order of $|\epsilon| = 0.1$ within the shear layer region. This region corresponds to the area where the convection velocity deviates most from the mean value assumed in Taylor's hypothesis, explaining the locally increased discrepancy. In the remaining part of the FOV a very good

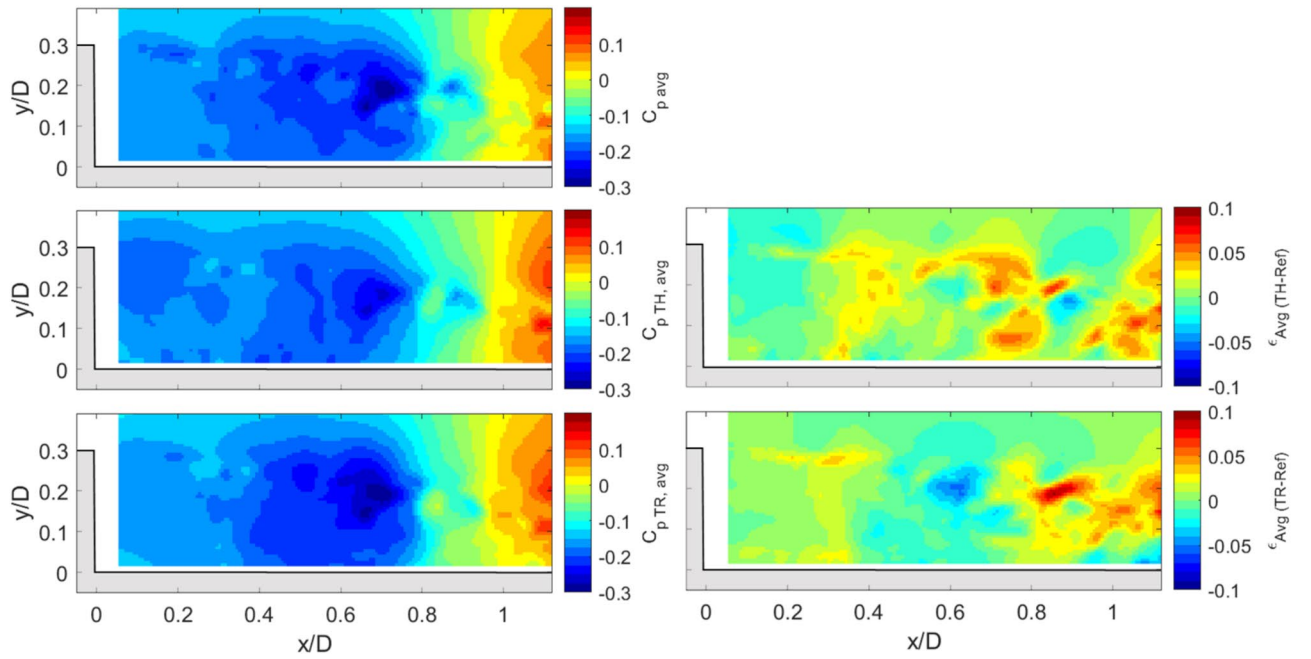

Fig. 6 Mean static pressure coefficient (synthetic data at $Ma = 0.7$) for reference data (top left), Taylor's hypothesis approach (center left) and time-resolved approach (bottom left). The discrepancies between the TH reconstruction and the reference data (center right) and between the TR reconstruction and the reference data (bottom right) are also reported

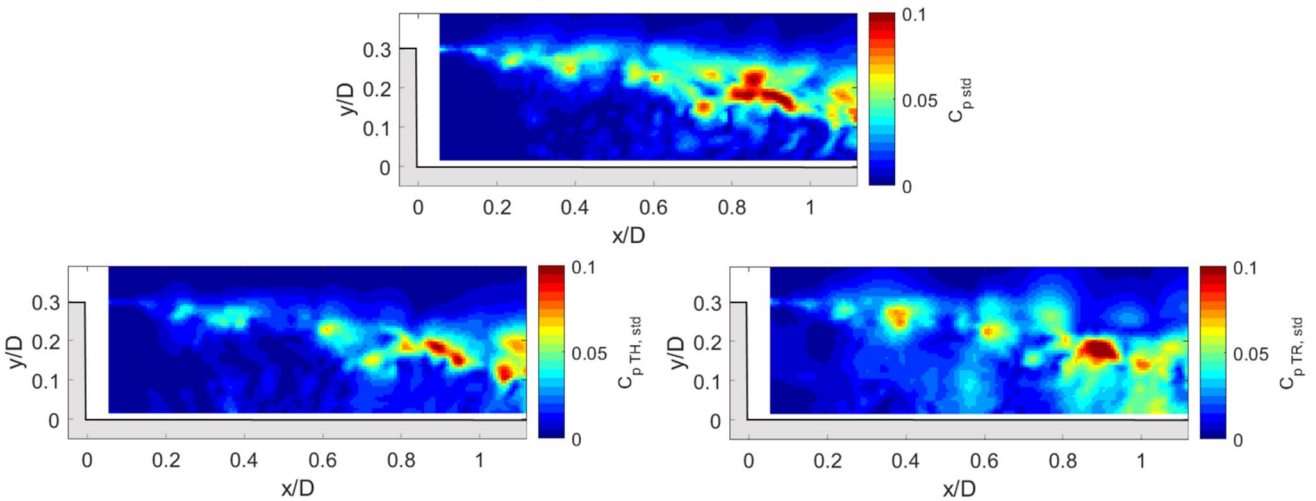

Fig. 7 Standard deviation of pressure coefficient (synthetic data at $Ma = 0.7$) for reference data (top), Taylor's hypothesis approach (bottom left) and time-resolved approach (bottom right)

agreement is observed, with $|\epsilon| < 0.03$. The TR method shows comparable error levels, although confined to a slightly smaller region.

The comparison of the mean pressure coefficient (Fig. 6) further confirms the capability of the TH approach to recover the average pressure field. The mean pressure maps were obtained by averaging the instantaneous reconstructed fields. The accuracy of the TH method in predicting the mean C_p distribution is comparable to that of the TR approach. The corresponding error maps (Fig. 6, right) indicate slightly higher discrepancies within the shear layer and near the reattachment region, while $|\epsilon| < 0.03$ in the rest of the field of view.

The standard deviation of the C_p field (Fig. 7) demonstrates that the TH approach also captures pressure fluctuations with good accuracy. Interestingly, in this restricted

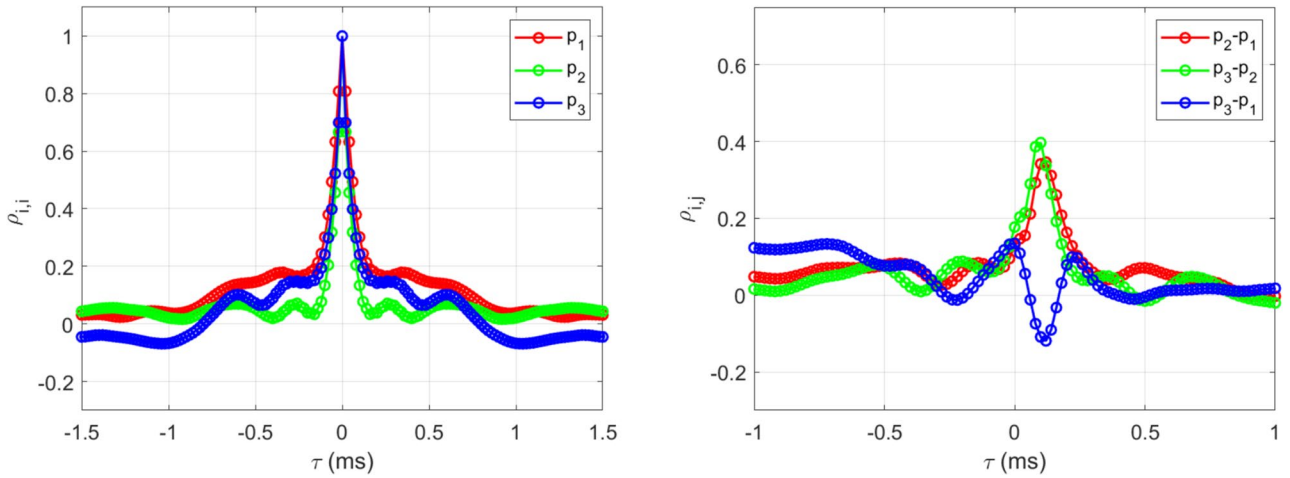

Fig. 8 Autocorrelation (left) and cross-correlation (right) of all pressure transducers for the launcher model

dataset (41 snapshots), the TR approach slightly overpredicts the spatial extent of the region with significant fluctuations. This behavior is consistent with the observations of van Gent et al. (2017), who analyzed the same dataset using different pressure reconstruction strategies. It should be noted, however, that their study employed volumetric data, thereby accounting for out-of-plane gradients.

Overall, this validation provides confidence that the Taylor's Hypothesis-based approach yields a reliable estimation of both instantaneous and statistical pressure fields. The largest discrepancies are observed within the shear layer, where deviations from the uniform convection assumption are expected. Nevertheless, the TH method produces results that are remarkably close to those obtained with an ideal time-resolved approach. This outcome supports the applicability of the TH-based reconstruction to real compressible experimental data, where time-resolved measurements are not available.

5 Pressure transducer data

Before addressing the PIV results on the VEGA-like launcher, some features of the pressure transducer measurements are discussed for the same experimental model. The objective of this section is to characterize the unsteady wall-pressure field and to extract preliminary information about the convection of pressure-carrying flow structures. These results provide a reference for the interpretation of the PIV-based pressure reconstruction presented in the following sections.

The pressure measurements were conducted simultaneously with the PIV measurements. However, the pressure transducers have a much higher acquisition frequency (50 kHz). To accurately synchronize the PIV images with the pressure transducer measurements, the triggering signal of the first laser pulse was recorded by a LabView program along with the signal of the pressure transducer. This allowed to obtain the value of the pressure transducer reading at the same time-instant as the PIV snapshot.

The main statistical values (mean and standard deviation) of the different pressure transducers will be discussed in conjunction with the analysis of the PIV data in Sect. 6.

The entire dataset of pressure measurements (excluding the start-up and shut-down phases of the wind tunnel) was used for correlation analysis, taking advantage of the high acquisition frequency of the transducers. The autocorrelation of the three pressure transducers (Fig. 8, left) shows a clear maximum at $\tau = 0$ ms, but no other significant peaks, indicating that the pressure spectrum is not dominated by a single tonal component. Thus, the wall-pressure fluctuations are broadband in nature and are not governed by a single coherent oscillation frequency. The absence of secondary peaks suggests that the unsteadiness is primarily associated with convecting turbulent structures rather than with a strong global resonance or self-sustained periodic motion.

On the contrary, in Fig. 8 (right), the cross-correlation of the pressure signals between different transducers is presented. All cross-correlations exhibit a non-negligible degree of correlation, particularly those transducers closest to each other: p_2 with p_1 and p_3 with p_2. The red line (p_2-p_1) displays a peak at $\tau = 0.12$ ms, indicating that structures passing through the first pressure transducer at time step t_0 reach the second pressure transducer at $t = t_0 + 0.12$ ms. Considering a distance of 15 mm between the transducers, this corresponds to a convection velocity of 125 m/s ($\sim 0.49\ V_\infty$). For the green line, (p_3-p_2) the peak of the cross-correlation is found at a slightly lower value of $\tau = 0.10$ ms, which results in a convection velocity of 150 m/s ($\sim 0.59\ V_\infty$). At approximately the same time delay, the blue curve, representing

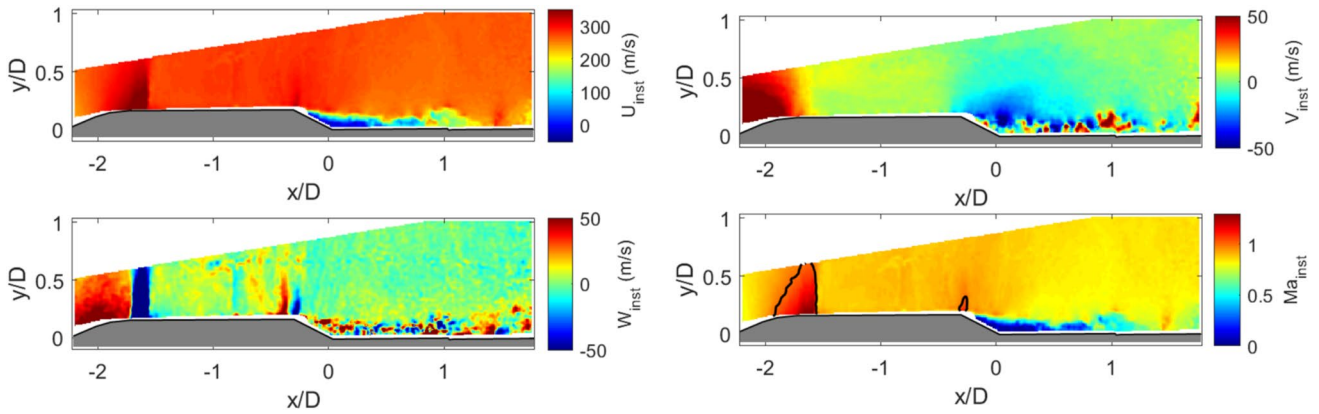

Fig. 9 Instantaneous PIV velocity and Mach number fields for $Ma = 0.8$, $\alpha = 0°$. Top left: streamwise velocity component; top right: vertical velocity component; bottom left: out-of-plane velocity component; bottom right: Mach number field with the $Ma = 1$ contour line indicated

the cross-correlation between the third and first pressure transducers, exhibits anti-correlation, although with a low correlation value (≈ -0.12), indicating a reduced coherence over the larger separation distance.

It is important to note that the convection velocity extracted from the cross-correlation represents the propagation speed of pressure-carrying flow structures along the wall. This convection velocity does not necessarily coincide with the local mean flow velocity at the wall, which is constrained by the no-slip condition. Instead, it reflects the advection speed of coherent structures within the boundary layer or shear layer that imprint their signature on the wall-pressure field. A more detailed comparison with the velocity field obtained from PIV will be provided in Sect. 6.2.

Overall, this correlation analysis indicates that the wall-pressure field is characterized by broadband unsteadiness and by downstream-convecting structures with a characteristic convection velocity in the range of 125–150 m/s. These results provide a first estimate of the relevant convection speed, which is later used to interpret the PIV measurements and the pressure reconstruction based on Taylor's hypothesis.

6 PIV-based pressure results

6.1 Instantaneous pressure field

Before examining the statistics of the pressure field on the launcher model, the performance of the pressure reconstruction algorithm for instantaneous snapshots is discussed. As anticipated in Sect. 3, all results presented in this study correspond to a freestream Mach number of 0.8 and angle of attack $\alpha = 0°$.

A typical instantaneous velocity field is depicted for the three velocity components in Fig. 9. In addition, the corresponding instantaneous Mach number distribution is shown in the same figure. The Mach number is computed from the magnitude of the instantaneous velocity vector, while the local speed of sound is evaluated assuming ideal-gas behavior and adiabatic flow conditions.

As the flow approaches the nose region, it first decelerates toward the stagnation point on the nose, where the velocity locally approaches zero. Downstream of this stagnation region, the flow accelerates along the curved surface of the ogive nose and eventually reaches locally supersonic conditions (see $Ma_{inst} = 1$ contour line in Fig. 9, bottom right). The flow expands further over the shoulder of the ogive nose until a quasi-normal shockwave is formed decelerating it again to subsonic conditions. In the nose area a positive velocity is observed for the vertical component (V_{inst}) as expected. Surprisingly, although the model is axisymmetric, the out-of-plane velocity component (W_{inst}) in this location shows a large non-zero velocity contribution. This is attributed to optical aberration effects due to the presence of the shock (see Elsinga et al. (2005)). In a stereo-PIV configuration, the W component is reconstructed from the disparity between the two camera views; therefore, even small asymmetric beam-steering effects along the optical paths may be interpreted as apparent out-of-plane motion. In contrast, the in-plane components are comparatively less affected.

When reaching the boat tail, a small secondary supersonic area is observed, again accompanied by aberration effects in the out-of-plane velocity component. The streamwise velocity component illustrates the presence of a separation region, extending less than a diameter downstream of the boat tail trailing edge. The boat tail geometry induces a negative vertical velocity and the shedding of vortices, most prominently visualized by the vertical and out-of-plane velocity component.

The in-plane material derivative is obtained by applying Eqs. 6 and 7 and shown in Fig. 10. It reveals distinct flow

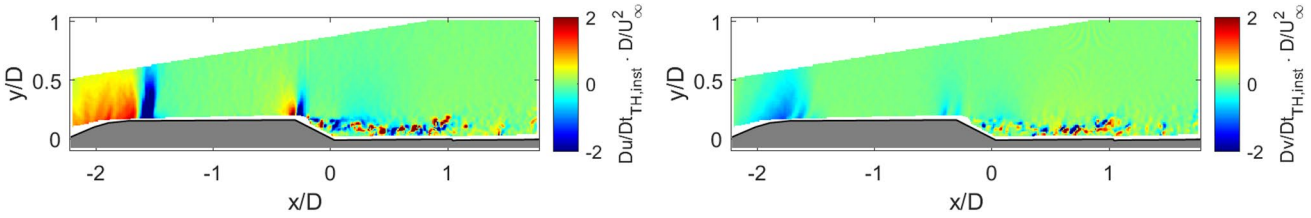

Fig. 10 Instantaneous material derivative for streamwise (left) and vertical (right) components

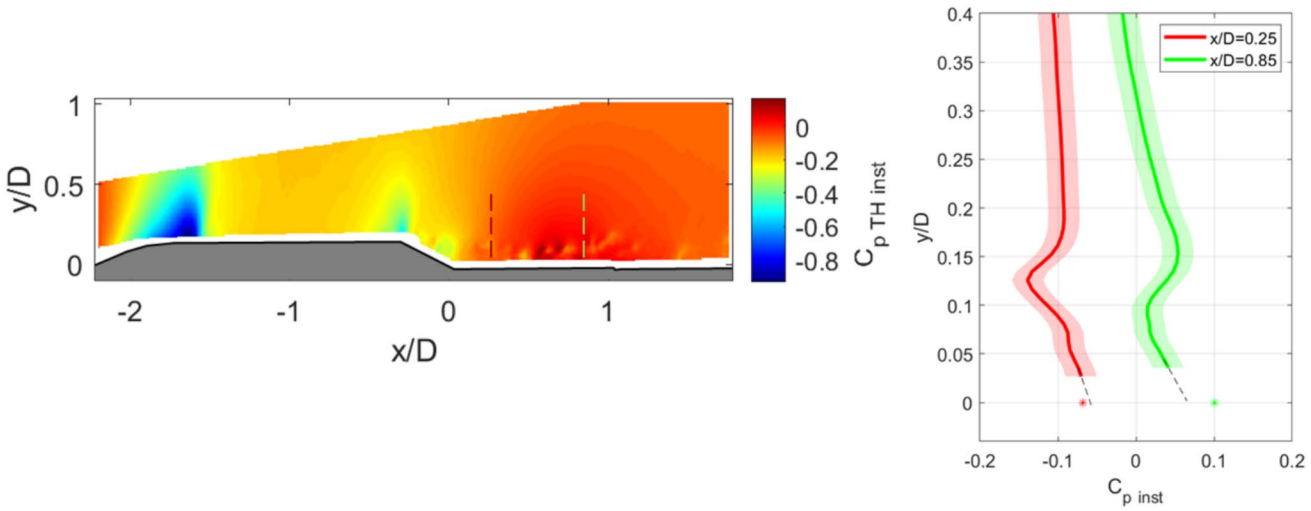

Fig. 11 Instantaneous pressure coefficient (left) and profiles at pressure transducer positions (right). For $y/D = 0$, the values obtained from transducer data are indicated with "*". The shaded regions represent the estimated uncertainty of the PIV-based pressure coefficient (± 0.02)

structures corresponding to expansion where the derivative is positive (representing flow acceleration) and compression regions indicated by negative values. Both material derivative components also clearly depict small scale structures with high local acceleration values corresponding to the vortical structures in the separation area.

Subsequently the Poisson equation (Eq. 8) is applied to the material derivative of Fig. 10 and the (instantaneous) pressure coefficient field is obtained and shown in Fig. 11. A negative pressure coefficient is present in the expansion region at the model shoulder ($-2 < x/D < -1.6$). As expected, a steep positive jump in pressure is observed across the adjacent shockwave structure. A second expansion region is also found just upstream of the boat tail, in agreement with Fig. 10. Further downstream, an increased pressure region occurs near the reattachment location ($x/D = \sim 0.3$), while also the imprint of vortex shedding can be observed in the pressure field. More details about these flow features will be provided in Sect. 6.2, along with the mean and standard deviation values.

To assess the accuracy of the PIV-based pressure field, Fig. 11 (right) compares transducer data at the model surface ('*' markers at $y/D = 0$) with PIV-based pressure profiles at the same x/D locations. As indicated in Sect. 3.2, the second transducer (p_2, $x/D = 0.55$) provided only pressure fluctuations, not absolute values. Accordingly, in all subsequent figures and discussions, absolute pressure profiles (with corresponding transducer values) are shown only for $x/D = 0.25$ (p_1) and $x/D = 0.85$ (p_3), while fluctuations are also reported at $x/D = 0.55$.

At $x/D = 0.25$, the difference between the transducer $C_{p\,\mathrm{inst}}$ and the PIV-based estimate at the bottom edge of the PIV field is small ($\Delta C_{p\,\mathrm{inst}} < 0.005$), whereas at $x/D = 0.85$ the discrepancy is larger ($\Delta C_{p\,\mathrm{inst}} \approx 0.06$). Part of this difference arises as in the current PIV setup laser reflections occur at the surface and disable the determination of velocities near the wall. Application of a linear extrapolation of the last points of the PIV pressure profile up to the launcher surface (for $0 < y/D < 0.02$) reduces the difference at $x/D = 0.85$ to $\Delta C_{p\,\mathrm{inst}} \approx 0.03$, i.e. about half of the non-extrapolated value. While this linear extrapolation provides a first-order estimate of the wall-pressure level, its accuracy is expected to decrease in regions where a thin shear layer develops in close proximity to the launcher surface and strong wall-normal pressure gradients are present (as for $x/D = 0.85$).

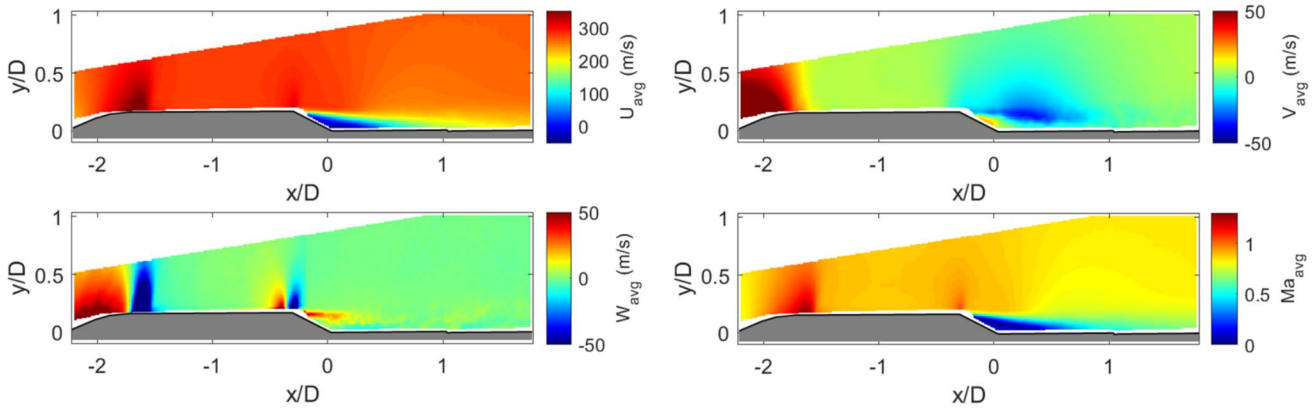

Fig. 12 Mean velocity field for streamwise (top-left), vertical (top-right), out-of-plane (bottom-left) components and mean Mach number field (bottom-right)

In the figures, the PIV-based pressure profiles are accompanied by a shaded uncertainty band (± 0.02) representing the estimated propagation of velocity uncertainties into the pressure coefficient, as estimated in Sect. 3.2.

Beyond the surface comparison, the wall-normal pressure distributions provide further insight into the local flow physics. At $x/D = 0.25$, the pressure coefficient remains nearly constant at approximately $Cp \approx -0.10$ within the region $0.17 < y/D < 0.40$. Moving closer to the wall, a local minimum is observed, with $Cp \approx -0.14$ at $y/D \approx 0.13$, associated with the influence of the separated shear layer. Subsequently, the pressure increases again toward the launcher surface, reaching an extrapolated value of approximately $Cp \approx -0.07$ at $y/D = 0$, in good agreement with the transducer measurement.

At $x/D = 0.85$, the wall-normal distribution exhibits a different behavior. Starting from the outer flow, the pressure coefficient decreases from approximately $C_p \approx -0.02$ at $y/D \approx 0.40$ to values close to $C_p \approx 0.05$ at $y/D \approx 0.15$. A local minimum is then observed within the range $0.05 < y/D < 0.15$, with a value of about $C_p \approx 0.01$ at $y/D \approx 0.10$. Approaching the wall, the pressure increases further, consistent with the recovery of static pressure in the reattachment region and in agreement with the surface transducer data.

These wall-normal distributions demonstrate the capability of the PIV-based methodology to capture the spatial evolution of the pressure field, providing detailed information that cannot be obtained from discrete pressure sensors alone.

6.2 Flow field statistics

The mean velocity and Mach number fields (Fig. 12) display very similar main flow features to those discussed for the instantaneous fields (Fig. 9).

A combined view of the three velocity components further clarifies the main flow behavior. Although the field of view does not include the upstream region where the flow decelerates and reaches a stagnation point at the nose center, this behavior precedes the acceleration observed along the nose. Further downstream along the nose region, all components indicate a strong disturbance: the streamwise velocity reveals an expansion and a shock-induced deceleration, while the vertical velocity shows a positive motion directed away from the surface indicating the displacement effect. A further upward velocity (together with reduced values of U_{avg}) is also present along the boat tail (for $-0.1 < x/D < 0$), The presence of the recirculation bubble is visible from the velocity field close to the boat tail (for $-0.1 < x/D < 0$), indicated by the altering vertical velocity component and reduced streamwise velocity. Further downstream the vertical component becomes largely negative due to the expansion induced by the boat-tail geometry. Out-of-plane velocities are close to zero across the FOV, except for localized deviations in expansion, compression, and in the shear layer, where optical aberrations can affect measurements.

The mean Mach number field clarifies the presence of a local supersonic region just downstream of the shoulder of the nose cone ($x/D = -2$ to -1.7), followed by a shockwave at an average position of $x/D = -1.7$.

In this averaged representation, the second supersonic region near the boat-tail remains visible, but barely ($Ma_{avg} \sim 1.05$), followed by only a small recompression region downstream. The figure further shows that the field of view fully captures the separated flow region, including the mean reattachment location at $x_{reat}/D = 0.31$ (computed as the end of the average reverse flow region near the model surface). It should be noted that the reattachment location is referenced with respect to the boat-tail bottom corner and therefore differs from the total separation length. Since separation initiates further upstream along the boat tail, a total

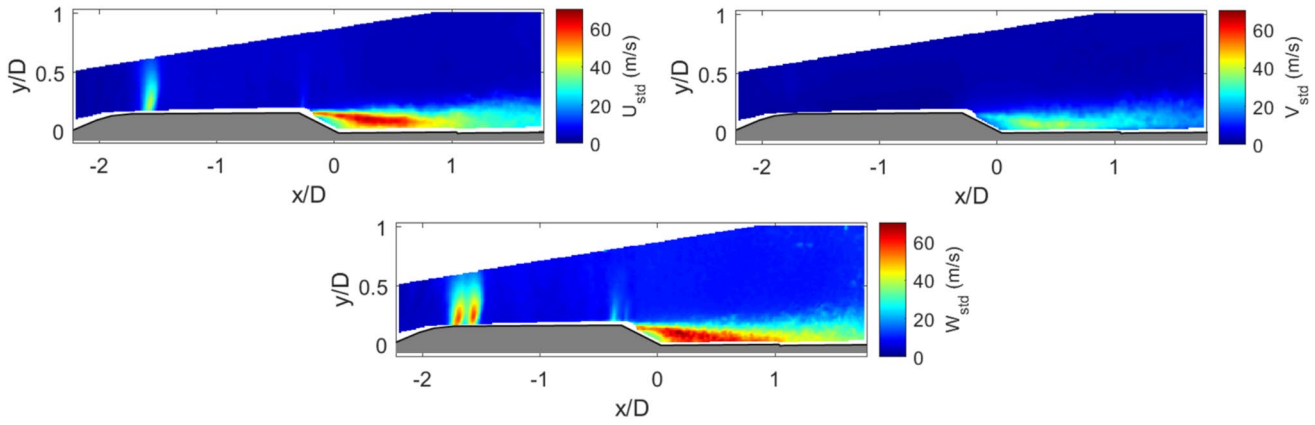

Fig. 13 Standard deviation field for streamwise (top-left), vertical (top-right) and out-of-plane (bottom) components

separation length (Δx_{sep}) of 0.50D, or 2.8h (step height of 9 mm), is obtained. This value is lower than those reported in literature for the Coe and Nute configuration (4.5h in *D'Aguanno* et al. (2025)) and for axisymmetric BFS cases (~ 3h, Schrijer et al. (2014); 3.5h, Scharnowski and Kähler (2015)). The difference with the Coe and Nute geometry cannot be attributed solely to the boat-tail angle (30° in the present configuration versus approximately 34° for Coe and Nute), but rather to a combination of geometric and flow-field effects. In particular, the VEGA-like model features a more gradual axial variation of the boat-tail slope, resulting in a smoother curvature distribution, while differences in the forebody geometry, especially the nose shape, influence the upstream shock structure and boundary-layer development prior to separation. In the Coe and Nute configuration, a stronger upstream shock system is observed, which modifies the incoming boundary layer and promotes a longer separation region. In contrast, the weaker shock structure in the present configuration leads to different inflow conditions at the boat-tail shoulder and a consequently shorter separation length.

Finally, it should be noted that, due to averaging, the small-scale vortical structures visible in the instantaneous fields (Figs. 9 - 11) are no longer discernible in the mean flow (Fig. 12).

To characterize the dynamics of the velocity field, the strength of the fluctuations of the three velocity components (in terms of standard deviation) is depicted in Fig. 13. Both the streamwise and out-of-plane velocity components exhibit significant fluctuations due to small oscillations of the first shockwave structure, differential slip of the seeding particles due to a certain particle diameter range, as well as optical aberrations. Corresponding fluctuations are not observed for the vertical velocity component. Fluctuations in the secondary shockwave structure are barely visible in the standard deviation fields of the streamwise and out-of-plane velocity components, indicating its almost fixed location.

All three velocity components highlight a high level of unsteadiness in the separation area including the shear layer. However, it is interesting to note that fluctuations are small close to the wall of the boat tail, suggesting a relatively steady recirculation involving low velocities. In the separation region the magnitude of the out-of-plane velocity fluctuations is of a similar order of magnitude as that for the streamwise component, whereby fluctuations of the vertical component are significantly lower. This implies that including or excluding the out-of-plane velocity component for pressure reconstruction could have a noticeable impact. Therefore, a more detailed analysis of this effect is needed and will be discussed in Sect. 6.3.

Regarding the material derivative, Fig. 14 displays the average value (left) and standard deviation (right) of both the streamwise and vertical components. For the mean fields, the streamwise component (top) shows negative values in correspondence with the shockwave structures, while, as expected, positive values are observed in the expansion regions. In contrast, the vertical component (bottom) primarily exhibits negative values within the expansion regions, while the shockwave structures, being nearly normal, are not clearly captured in this component. This difference reflects the dominant alignment of the shock-induced gradients with the streamwise direction. For the standard deviation fields, the streamwise contribution highlights increased levels within the oscillation region of the primary shockwave, as well as pronounced fluctuations in the separated shear layer and wake region, where the highest levels of unsteadiness are present. The vertical component, on the other hand, does not show significant fluctuations in the shockwave region, but exhibits noticeable fluctuations in the separated and wake regions. These extend over a similar spatial extent as in the streamwise component, although with lower peak values.

The corresponding average pressure field, obtained by averaging all the instantaneous pressure snapshots, is shown in Fig. 15 (top left). Similar to the instantaneous field, the

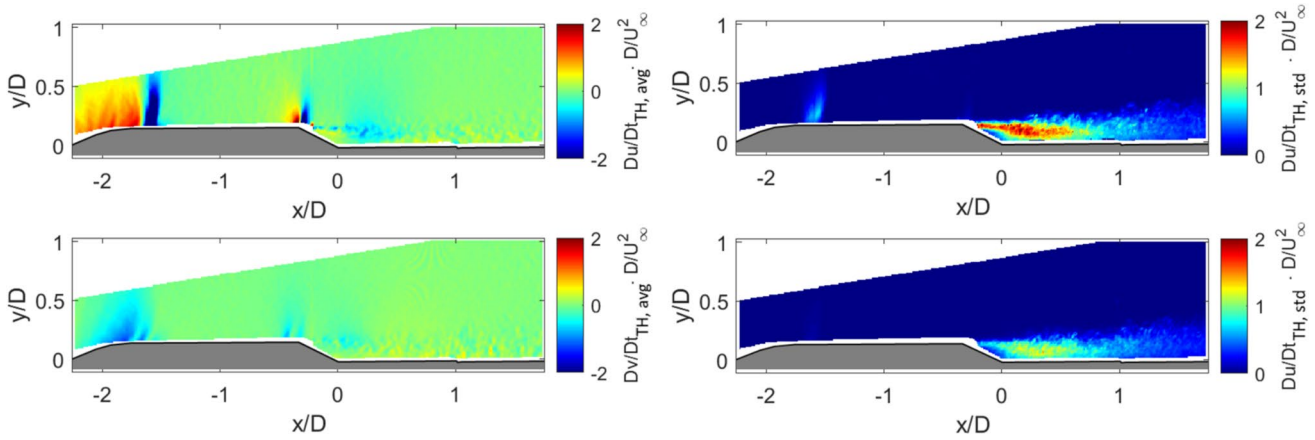

Fig. 14 Mean (left) and standard deviation (right) of streamwise (top) and vertical (bottom) components of the material derivative

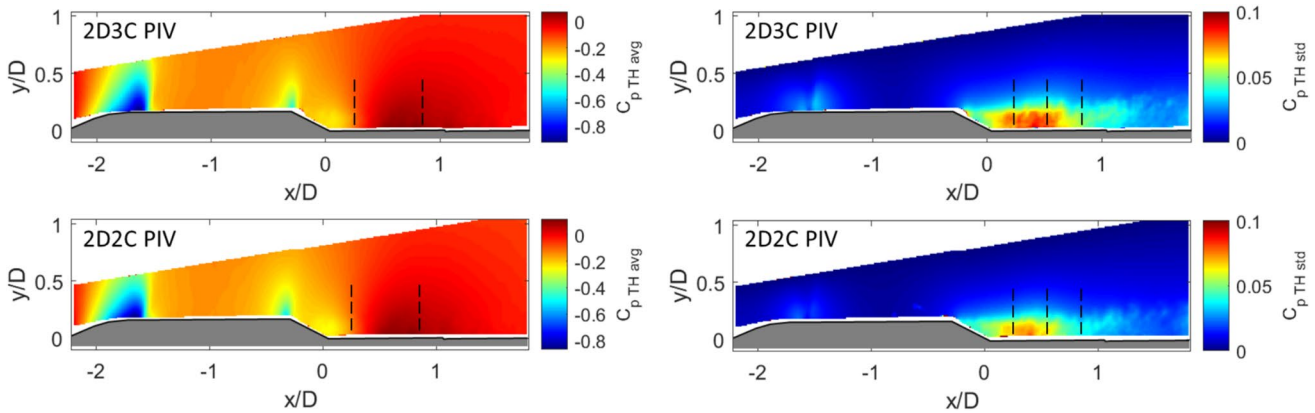

Fig. 15 Mean pressure coefficient (left) and relative standard deviation (right) fields, for stereo-PIV (top) and planar-PIV data (bottom)

average field displays low pressure coefficient values in the supersonic regions, which are terminated by shock waves, and shows compression in the reattachment region. Considering the standard deviation of the pressure coefficient (Fig. 15, top right), the main pressure fluctuations appear in close proximity to the primary shock and in the separation area. The bottom row of diagrams shows the corresponding results for the pressure reconstruction procedure when only planar data are taken into account; this will be discussed in more detail in Sect. 6.3.

It is interesting to note that, while the fluctuations of the streamwise material derivative (see Fig. 14, right) have the highest intensity in the shear layer, the largest fluctuations in the pressure field are actually experienced closer to the wall. This behavior reflects the non-local nature of the pressure field, which results from the combined effect of material-derivative contributions, density variations, and boundary conditions through the Poisson formulation, so that regions of maximum pressure fluctuations do not necessarily coincide with regions of maximum source-term intensity.

To discuss the accuracy of the pressure reconstruction procedure on the main statistics, wall-normal profiles of both the average and the standard deviation fields of C_p are shown in Fig. 16 for the streamwise locations where the unsteady pressure transducers are located ($x/D = 0.25, 0.55, 0.85$, locations marked with a dashed black line in Fig. 15). To assist the interpretation of these profiles, the corresponding streamwise velocity profiles are also reported in Fig. 17.

As expected, negative values of the pressure coefficient are obtained at $x/D = 0.25$ (p_1) along the entire profile, consistent with the instantaneous profile shown in Fig. 11 (right). At that position, a region of reverse flow is still present, as illustrated in Fig. 12 and Fig. 17 (left). This partially explains why the discrepancy between the reconstructed and transducer-measured mean pressures is slightly larger in this region. Overall, the average surface pressure values measured by the transducers show acceptable agreement with those reconstructed from the velocity data. When applying a linear extrapolation of C_p up to the launcher surface, a difference of $\Delta C_{p\,\mathrm{avg}} \approx 0.03$ is obtained at $x/D = 0.25$, while

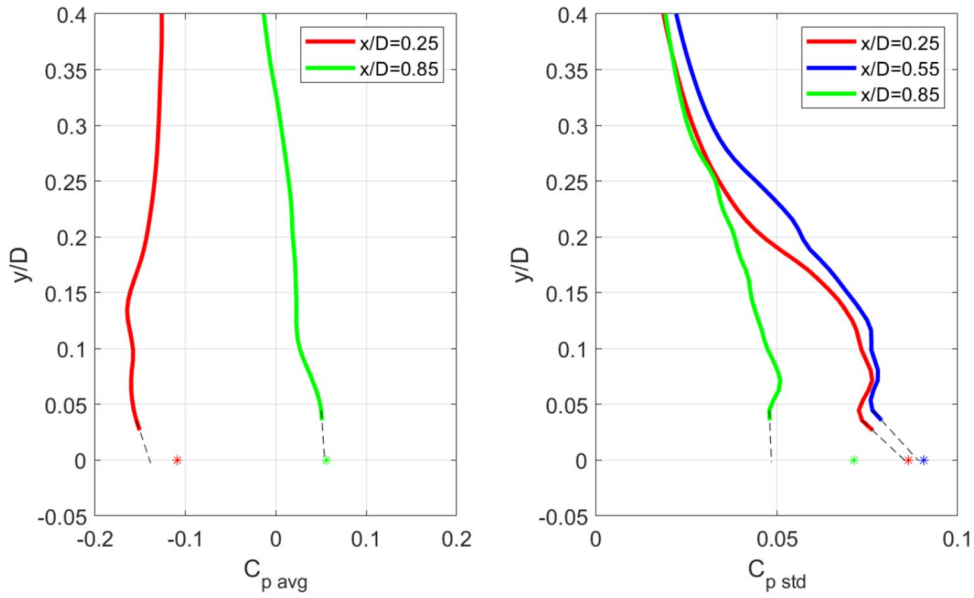

Fig. 16 Mean (left) and standard deviation (right) of the pressure coefficient profiles in correspondence with pressure transducer positions

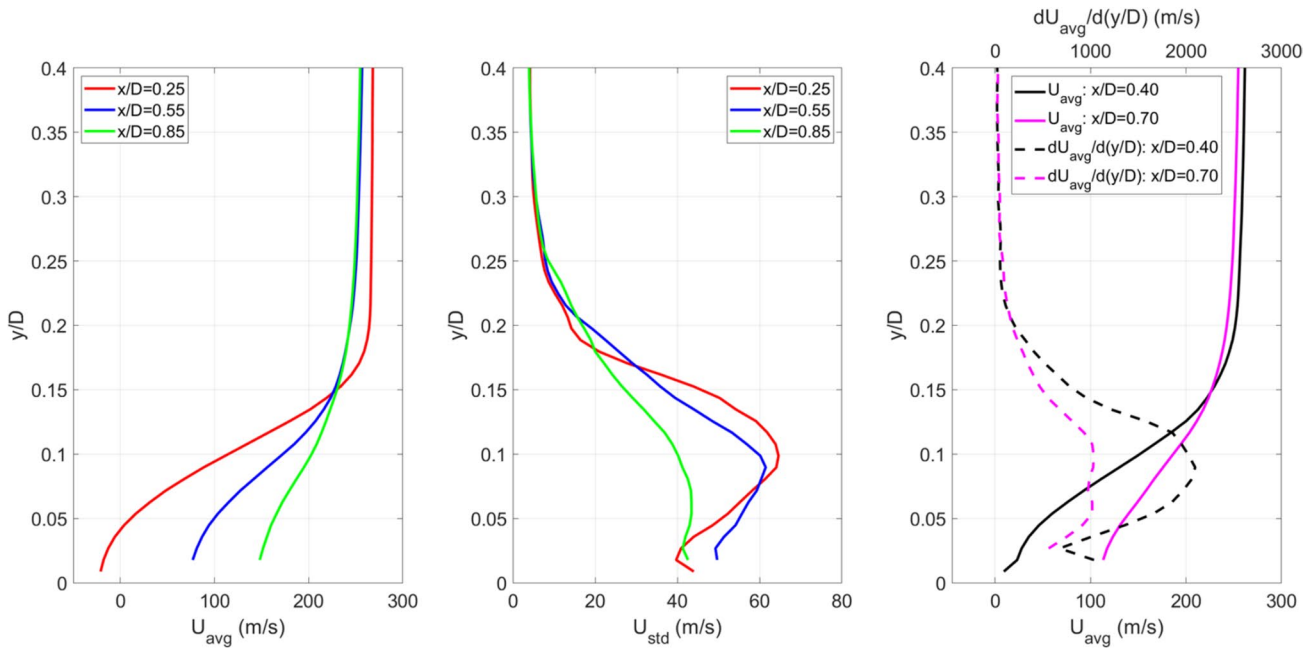

Fig. 17 Mean (left) and standard deviation (center) of the streamwise velocity profiles in correspondence with pressure transducer positions. On the right, the profiles of mean velocity and of velocity gradient are shown for $x/D = 0.40$ and $x/D = 0.70$ (locations in between the pressure transducers)

a much smaller difference of $\Delta C_{p\,\mathrm{avg}} \approx 0.002$ is observed at $x/D = 0.85$ (p_3).

In terms of pressure fluctuations, higher values for the standard deviation are observed at p_1 and p_2. This is because the reattachment region covers the positions of these two pressure transducers and thereby associates the highest velocity fluctuations, as shown in Fig. 17 (center).

Obviously, the velocity-based reconstruction generally underestimates the pressure fluctuations. The largest discrepancy (ΔC_p) between the reconstructed and transducer-measured values occurs at $x/D = 0.85$ ($\Delta C_{p\,\mathrm{std}} \approx 0.033$), while for $x/D = 0.25$ ($\Delta C_{p\,\mathrm{std}} \approx 0.010$) and $x/D = 0.55$ ($\Delta C_{p\,\mathrm{std}} \approx 0.012$), the agreement is much closer. This difference is mainly attributed to the lack of information near the model surface, as also discussed in Sect. 6.1. For example, at the location

of transducer p_3 ($x/D = 0.85$), the shear layer is relatively thin, and the associated fluctuations occur in a region that is partially inaccessible to the PIV measurements due to laser reflections. In contrast, at locations where the transducers are fully immersed in the separation region, the unsteadiness at the bottom of the PIV field of view is more comparable to that measured by the pressure transducers at the surface.

This observation is further confirmed, if a linear extrapolation of the PIV-derived pressure fluctuations up to the launcher surface is applied. For p_1 and p_2, the extrapolated values provide an excellent estimate ($\Delta C_{p\,\mathrm{std}} \approx 0.001$), while for p_3 at $x/D = 0.85$ ($\Delta C_{p\,\mathrm{std}} \approx 0.032$), a significant discrepancy remains.

A further point of interest is the comparison between the mean velocity estimated from the PIV velocity field (Fig. 12) and the convection velocity inferred from the unsteady pressure measurements (Sect. 5). In the present study, Taylor's hypothesis is applied assuming $U_c = U_{\mathrm{avg}}$, i.e., that the local mean streamwise velocity is representative of the convection velocity of dominant flow structures.

To assess the validity of this assumption at the locations of the pressure transducers (aligned in the streamwise direction), the convection velocities obtained from the cross-correlation between transducers p_1-p_2 and p_1-p_3 (Sect. 5) are compared with the mean velocity profiles extracted at the mid-distance between adjacent sensors (respectively at $x/D = 0.40$ and $x/D = 0.70$).

Since the dominant pressure fluctuations are associated with structures convected within the separated shear layer, the wall-normal distributions of the mean streamwise velocity and its gradient were examined at these locations to identify the shear-layer region (Fig. 17, right). The shear layer is identified based on the presence of an inflection point in the mean velocity profile, i.e. a location where the second derivative changes sign. This region is typically associated with a peak in the velocity gradient and represents a classical indicator of shear-layer instability (Rayleigh's inflection point criterion).

At $x/D = 0.40$, the inflection point of the mean velocity profile is located at $y/D \approx 0.09$, corresponding to a local velocity of approximately 130 m/s. This value is in close agreement with the convection velocity inferred from the pressure cross-correlation (125 m/s, see Sect. 5). Further downstream ($x/D = 0.70$) a shear-layer region in the range $0.05 < y/D < 0.10$, within which the velocity ranges between 135 and 180 m/s, is observed. Although the inflection point is less sharply defined at this location, the region of elevated velocity gradient still identifies the shear layer region. The convection velocity extracted from the pressure measurements (150 m/s) falls within this interval, supporting the interpretation that the dominant pressure-carrying structures convect within the separated shear layer rather than in the near-wall reverse-flow region.

It should also be noted that the convection velocity obtained from transducers cross-correlation is inherently discrete due to the finite sensor spacing and sampling frequency. Given the transducer separation of 0.015 m and the acquisition frequency of 50 kHz ($\Delta t = 20$ µs), the admissible convection velocities follow the relation $U_c = 0.015/\tau$, where $\tau = n\Delta t$ is the discrete time lag corresponding to the correlation peak. Consequently, only discrete velocity levels (e.g., 94, 107, 125, 150, 187.5 m/s) can be identified. The slight differences observed between the PIV-derived shear-layer velocities and the correlation-based convection velocities are therefore partly attributable to this discretization.

Finally, the measured pressure fluctuations reflect the footprint of coherent structures convected in the outer shear layer (although the first transducer is located within the reverse-flow region of the separation bubble). Since pressure is obtained from a Poisson equation, which is elliptic in nature, its fluctuations depend on the spatial distribution of the source terms over the entire flow field and are therefore not solely determined by the local mean velocity. As a result, the wall-mounted pressure sensors can capture the influence of shear-layer structures even in regions where the local mean velocity is small or negative.

6.3 Effect of the out-of-plane velocity component on pressure reconstruction

A final analysis is made to characterize the effect of the out-of-plane component on the pressure estimation. The particular purpose of this assessment is to estimate to what extent the results of the stereo approach compare with the planar approach, since the latter is simpler and hence more applicable in industrial environments with limited optical access. Note that from a mathematical point of view the difference between 2D2C and 2D3C PIV for pressure determination (in a plane) is the inclusion of the out-of-plane velocity component which contributes to the velocity magnitude ($|V|$), that appears in the denominator of Eqs. 6 and 7.

To demonstrate the effect of the out-of-plane velocity component, Fig. 15 shows the pressure coefficient field for both PIV processing procedures, the stereo approach on top and the planar approach below. For the 2D2C PIV (bottom row) only the raw images from camera 1 and camera 3 (see the PIV setup in Fig. 4, right) are considered.

Concerning the mean pressure coefficient, the results of both approaches are pretty similar in the entire field of view with a maximum difference in $C_{p\,\mathrm{avg}}$ of 0.03. However, for the standard deviation of the pressure fluctuations some important differences are visible in the separation area. The 2D2C PIV based pressure fields (Fig. 15, bottom) return values of $C_{p\,\mathrm{std}}$, that are approximately 0.02 lower than the values from the 2D3C PIV data (Fig. 15, top). These differences may be attributed to the neglect of the out-of-plane

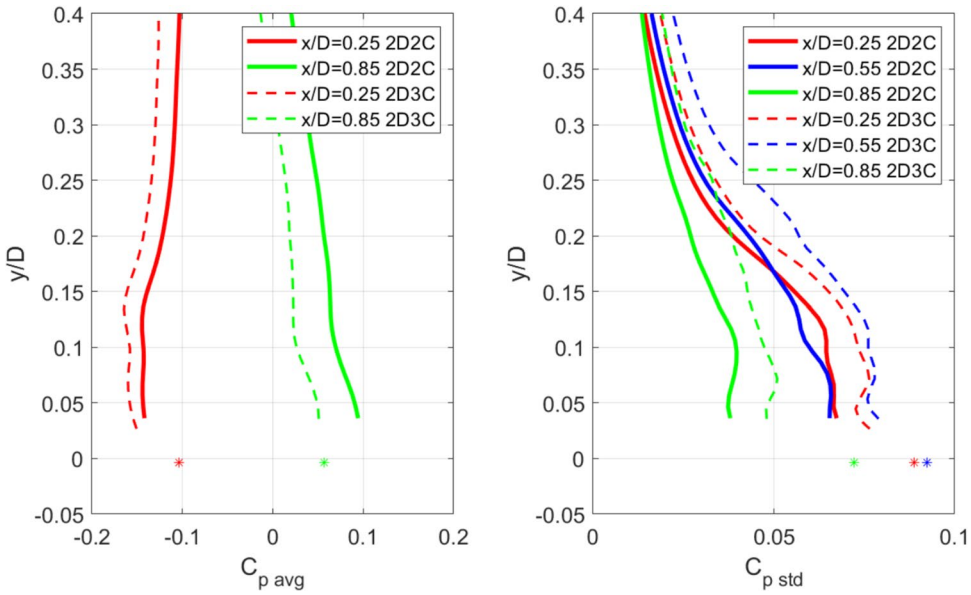

Fig. 18 Mean (left) and standard deviation (right) of pressure coefficient profiles for 2D2C (solid lines) and 2D3C (dashed lines) PIV data

velocity fluctuations in the 2D2C approach, which are particularly intense in the separation area downstream of the boat tail (see Fig. 13, bottom). Additionally, stereo-PIV is generally more sensitive to measurement noise, especially in the reconstructed out-of-plane component. While this may only marginally increase the reconstructed pressure fluctuation levels, the dominant contribution is expected to arise from the inclusion of the out-of-plane velocity component in the pressure evaluation.

To further clarify the impact of the out-of-plane velocity component, Fig. 18 compares wall-normal profiles of the mean pressure coefficient and its standard deviation obtained from the 2D2C and 2D3C processing. The mean C_p profiles indicate a slightly lower agreement between the pressure transducer measurements and the PIV-based reconstruction when the 2D2C data are used, compared to the 2D3C case, particularly at $x/D = 0.85$. At $x/D = 0.25$, the agreement is comparable, with the 2D2C data appearing slightly closer to the transducer value at the lowest measured point. However, when considering the extrapolated pressure towards the wall (not explicitly shown in the figure for clarity), the 2D3C reconstruction provides a closer estimate of the surface pressure. These observations indicate that including the out-of-plane velocity component improves the pressure estimation, particularly in regions of stronger three-dimensionality and when estimating near-wall pressure levels.

The comparison of the standard deviation profiles further highlights this difference: at all three locations ($x/D = 0.25$, 0.55, and 0.85), the 2D2C reconstruction systematically underestimates the pressure fluctuation levels relative to both the pressure transducers and the 2D3C results. This behavior is consistent with the fact that the transducers are positioned within a region where significant out-of-plane velocity fluctuations are present and are not accounted for in the 2D2C pressure evaluation.

7 Conclusions

This investigation presented an approach for reconstructing instantaneous pressure from non-time-resolved PIV data, enabling the estimation of unsteady pressure fluctuations e.g. around launcher fairing configurations under compressible (transonic) flow conditions. The primary objective of developing a validated methodology robust enough for application in industrial wind tunnel facilities, has been successfully achieved.

Validation using synthetic data demonstrated that the Taylor's hypothesis approach has an average error in C_p of approximately $\Delta C_p \approx 0.01$, compared to an ideal Eulerian time-resolved approach.

The single-snapshot approach using Taylor's hypothesis was then applied to reconstruct the pressure under experimental compressible conditions, showing quantitative consistency with the pressure transducers for both instantaneous and mean pressure values. The range of discrepancy at the two available transducer locations in terms of mean C_p is $\Delta C_{p\,\mathrm{avg}} \approx 0.002$–$0.02$, consistent with the error magnitude obtained from the synthetic data validation. Slightly larger differences are observed in the comparison of the standard deviation of C_p ($\Delta C_{p\,\mathrm{std}} \approx 0.01$–$0.03$).

A structured assessment of the experimental discrepancies indicates that the total ΔC_p arises from multiple contributions of comparable order. One important aspect is certainly associated with the accuracy of the Taylor's hypothesis and of the approximation of the convection

velocity with the mean PIV velocity. However, the comparison of the convection velocity as inferred from the pressure transducers is within 5–10% of the measured mean velocity at the core of the shear layer, where most of the vortical flow structures are convected. In addition to the intrinsic TH approximation (computed as corresponding to an error in C_p of ~ 0.01 from the synthetic data), the neglect of fully three-dimensional velocity gradients may contribute significantly in regions of strong three-dimensionality. While inclusion of the out-of-plane velocity component (as inferred from the comparison between planar and stereo reconstructions) does not significantly alter the shape of the mean pressure field, it affects the absolute C_p levels and improves the estimation of pressure fluctuations, particularly within the separation region (differences in $C_{p\,\mathrm{std}}$ of about 0.02).

Measurement-related velocity uncertainties introduce an additional contribution. Given typical PIV uncertainty levels of approximately 1% of the local velocity magnitude, the propagated effect on the pressure coefficient is estimated to be on the order of $\Delta C_p \approx 0.01$–0.02. Particle lag effects are confined to limited regions near shock-wave oscillations and do not significantly influence the mean C_p comparison presented here. Finally, the absence of velocity information in a small region close to the model surface, caused by laser reflections and camera viewing constraints, introduces further uncertainty in the pressure integration. A first-order approximation of this missing information was obtained through linear extrapolation of the PIV-based C_p values onto the launcher surface. Although simplified, this procedure reduces part of the observed mismatch.

Overall, the experimental differences between PIV-based and transducer-based pressure estimates are consistent with the cumulative effect of these moderate contributions. No single mechanism dominates the total error budget, confirming the robustness of the proposed pressure reconstruction methodology under the investigated compressible flow conditions.

The experimental PIV data were also used to identify and analyze the key flow features characteristic of the hammerhead geometry: two distinct shockwave structures, a separation region downstream of the boat tail, and the subsequent reattachment zone. Flow reattachment occurs at a distance of roughly $0.5D$ ($2.8h$) from the boat-tail shoulder. This distance is reduced by about $0.3D$ compared to the Coe and Nute configuration, primarily due to the smoother transition from the payload to the boat-tail region in the VEGA-like model and to the different nose geometry.

The methodology is capable of pinpointing regions of the launcher subjected to high unsteady loads, which are particularly relevant in the separated boat tail region, with maximum values of $C_{p\,\mathrm{std}}$ ($C_{p\,\mathrm{std}} \approx 0.09$) present for $0.1 < x/D < 0.6$. Interestingly, pressure unsteadiness due to the first shockwave oscillations are much less significant, with peak values of $C_{p\,\mathrm{std}} \approx 0.04$, while no relevant fluctuation near the secondary shockwave structure was observed. Finite particle relaxation time may attenuate velocity fluctuations in regions with a high velocity gradient and thus reduce the reconstructed pressure variance, such as across the primary shock. However, the measured velocity standard deviation in the shock region is intrinsically lower than in the separated shear layer. This suggests that the comparatively small $C_{p\,\mathrm{std}}$ values near the primary shock primarily reflect the underlying flow dynamics, while particle-response effects may contribute only to a partial attenuation of high-frequency components.

The proposed methodology is not inherently restricted to subsonic and transonic conditions. The governing pressure reconstruction equation (Eq. 3) has previously been applied in supersonic flows with strong shocks, and Taylor's hypothesis remains applicable provided that convective transport dominates local unsteadiness. At higher Mach numbers, stronger velocity gradients may locally enhance particle-response and optical distortion effects, requiring careful uncertainty assessment. Similarly, at non-zero angles of attack, increased flow three-dimensionality amplifies the importance of measuring out-of-plane velocity components. In such cases, stereo or volumetric PIV approaches would further improve pressure reconstruction accuracy.

In conclusion, the results, particularly for the 2D3C case, demonstrate that the single-snapshot method is a highly attractive option for industrial compressible applications, where more complex PIV setups (e.g., dual-PIV or volumetric) or time-resolved measurements in high-speed conditions are often impractical due to technical limitations. Beyond its practicality, the method also provided valuable insights into the unsteady flow physics of transonic launcher configurations.

Acknowledgements The authors gratefully acknowledge Dr. Daniele Ragni for his insightful discussions regarding the pressure reconstruction methodology and the associated Poisson formulation.

Author contributions All authors contributed to the study conception, design and preparation. Data collection and analysis were performed by AD. The first draft of the manuscript was written by AD. AD, FS and BvO commented on previous versions of the manuscript. All authors read and approved the final manuscript.

Funding This work has been carried out as part of the project TUPLE (Transonic PIV based Unsteady Pressure measurements for Launcher Environment), funded by the European Space Agency, under contract nr. 4000139185.

Data availability Data that support the findings of this study are available on request from the corresponding author.

Declarations

Conflict of interest The authors declare no conflict of interest.

Ethical approval Not applicable.

References

Charonko JJ, King CV, Smith BL, Vlachos PP (2010) Assessment of pressure field calculations from particle image velocimetry measurements. Meas Sci Technol 21:105401. https://doi.org/10.1088/0957-0233/21/10/105401

Coe CF, and Nute JB, (1962) "Steady and fluctuating pressures at transonic speeds on hammerhead launch vehicles," Tech. rep. NASA TM X-778

D'Aguanno A, (2023) "Physics and Control of Transonic Buffet," PhD thesis, Delft University of Technology https://doi.org/10.4233/uuid:7e4f868b-7716-4c36-8fa0-b55572d1572b

D'Aguanno A, Gonzalez Romero A, Schrijer FFJ, van Oudheusden BW (2025) Flow analysis of hammerhead launcher geometries in the transonic regime. AIAA J 63(8):3297–3308. https://doi.org/10.2514/1.J064688

Davoust S, Jacquin L (2011) Taylor's hypothesis convection velocities from mass conservation equation. Phys Fluids 23(5):051701. https://doi.org/10.1063/1.3584004

de Kat R, Ganapathisubramani B (2013) Pressure from particle image velocimetry for convective flows: a Taylor's hypothesis approach. Meas Sci Technol 24:024002. https://doi.org/10.1088/0957-0233/24/2/024002

de Kat R, van Oudheusden BW (2012) Instantaneous planar pressure determination from PIV in turbulent flow. Exp Fluids 52(5):1089–1106. https://doi.org/10.1007/s00348-011-1237-5

Elsinga GE, van Oudheusden BW, Scarano F (2005) Evaluation of aero-optical distortion effects in PIV. Exp Fluids 39:246–256. https://doi.org/10.1007/s00348-005-1002-8

de Kat R, (2012) "Instantaneous planar pressure determination from particle image velocimetry," PhD Thesis, Delft University of Technology

van Gent PL, Gentile V, van Oudheusden BW, and Schrijer FFJ, (2016) "Experimental assessment of PIV/PTV-based pressure reconstruction techniques applied to a low-speed base flow," In International Workshop on Non-Intrusive Optical Flow Diagnostics

Geschwindner C, Westrup K, Dreizler A, Böhm B (2022) Ultra-high-speed time-resolved PIV of turbulent flows using a continuously pulsing fiber laser. Exp Fluids 63(4):75. https://doi.org/10.1007/s00348-022-03424-7

Ghaemi S, Ragni D, Scarano F (2012) PIV-based pressure fluctuations in the turbulent boundary layer. Exp Fluids 53:1823–1840. https://doi.org/10.1007/s00348-012-1391-4

Goin KL, and Pope A, (1965) "High-speed wind tunnel testing," New York, John Wiley and sons INC, p.320

Laskari A, de Kat R, Ganapathisubramani B (2016) Full-field pressure from snapshot and time-resolved volumetric PIV. Exp Fluids 57:44. https://doi.org/10.1007/s00348-016-2129-5

LaVision, (2017) "Flow Master Time-Resolved Particle Image Velocimetry Systems," https://www.lavision.de/en/downloads/brochures.php

Lin C (1953) On Taylor's hypothesis and the acceleration terms in the Navier–Stokes equations. Q Appl Math 10(4):295–306

Lynch KP, Scarano F (2014) Material acceleration estimation by four-pulse tomo-PIV. Meas Sci Technol 25:084005. https://doi.org/10.1088/0957-0233/25/8/084005

McClure J, Yarusevych S (2017) Optimization of planar PIV-based pressure estimates in laminar and turbulent wakes. Exp Fluids 58:62. https://doi.org/10.1007/s00348-017-2337-7

Panda J, Garbeff T, Burnside N, Ross J (2018) Unsteady pressure fluctuations measured on a hammerhead space vehicle and comparison with Coe and Nute's 1962 data. Int J Aeroacoust 17:70–87

Pröbsting S, Scarano F, Bernardini M, Pirozzoli S (2013) On the estimation of wall pressure coherence using time-resolved tomographic PIV. Exp Fluids 54:1567. https://doi.org/10.1007/s00348-013-1567-6

Ragni D, Schrijer FFJ, van Oudheusden BW, Scarano F (2011a) Particle tracer response across shocks measured by PIV. Exp Fluids 50:53–64. https://doi.org/10.1007/s00348-010-0892-2

Ragni D, van Oudheusden BW, Scarano F (2011b) Non-intrusive aerodynamic loads analysis of an aircraft propeller blade. Exp Fluids. https://doi.org/10.1007/s00348-011-1057-7

Scharnowski S, Kähler CJ (2015) Investigation of a transonic separating/reattaching shear layer by means of PIV. Theor Appl Mech Lett 5(1):30–34. https://doi.org/10.1016/j.taml.2014.12.002

Schreyer AM, Lasserre JJ, Dupont P (2015) Development of a Dual-PIV system for high-speed flow applications. Exp Fluids. https://doi.org/10.1007/s00348-015-2053-0

Schrijer FFJ, Sciacchitano A, Scarano F (2014) Spatio-temporal and modal analysis of unsteady fluctuations in a high-subsonic base flow. Phys Fluids. https://doi.org/10.1063/1.4891257

Schuster, D. M., Panda, J., Ross, J. C., Roozeboom, N. H., Burnside, N. J., Ngo, C. L., Sellers, M., and Powell, J. M., "Investigation of unsteady Pressure-Sensitive paint (uPSP) and a dynamic loads balance to predict launch vehicle buffet environments," Tech. Rep. NASA/TM-2016–219352, 2016.

Sciacchitano A, Scarano F (2014) Elimination of PIV light reflections via a temporal high pass filter. Meas Sci Technol 25(8):084009. https://doi.org/10.1088/0957-0233/25/8/084009

Souverein L, van Oudheusden BW, and Scarano F, (2007) "Particle image velocimetry based loads determination in supersonic flows," In 45th AIAA Aerospace Sciences Meeting and Exhibit, AIAA Paper 2024–2145 https://doi.org/10.2514/6.2007-50

Van der Kindere JW, Laskari A, Ganapathisubramani B, De Kat R (2019) Pressure from 2D snapshot PIV. Exp Fluids 60:1–18. https://doi.org/10.1007/s00348-019-2678-5

van Oudheusden BW (2008) Principles and application of velocimetry-based planar pressure imaging in compressible flows with shocks. Exp Fluids 45:657–674. https://doi.org/10.1007/s00348-008-0546-9

van Oudheusden BW (2013) PIV-based pressure measurement. Meas Sci Technol 24:032001. https://doi.org/10.1088/0957-0233/24/3/032001

van Oudheusden BW, Souverein L (2007) Evaluation of the pressure field from PIV in a shock wave boundary layer interaction, In 7th International Symposium on Particle Image Velocimetry Italy Rome

van Gent PL, Michaelis D, van Oudheusden BW, Weiss PÉ, de Kat R, Laskari A, Jeon YJ, David L, Schanz D, Huhn F, Gesemann S, Novara M, McPhaden C, Neeteson NJ, Rival DE, Schneiders JFG, Schrijer FFJ (2017) Comparative assessment of pressure field reconstructions from particle image velocimetry measurements and Lagrangian particle tracking. Exp Fluids 58:33. https://doi.org/10.1007/s00348-017-2324-z

van Gent PL, van Oudheusden BW, Schrijer FFJ (2018) Determination of mean pressure from PIV in compressible flows using the Reynolds-averaging approach. Exp Fluids 59:41. https://doi.org/10.1007/s00348-018-2487-2

van Oudheusden BW, Scarano F, Roosenboom EWM, Casimiri EWF, Souverein LJ (2007) Evaluation of integral forces and pressure fields from planar velocimetry data for incompressible and compressible flows. Exp Fluids 43:153–162. https://doi.org/10.1007/s00348-007-0261-y

Authors and Affiliations

A. D'Aguanno[1,2] · F. F. J. Schrijer[1] · B. W. van Oudheusden[1]

✉ A. D'Aguanno
alessandro.daguanno@vki.ac.be

[1] Department of Flow Physics and Technology, Delft University of Technology, Kluyverweg 1, 2629 HS Delft, The Netherlands

[2] Turbomachinery and Propulsion Department, von Karman Institute for Fluid Dynamics, Waterloosesteenweg 72, 1640 Sint-Genesius-Rode, Belgium